Numerical simulation of wave propagation in finely layered and attenuated medium*

Lawrence H. T. Le and Robert Burridge**

ABSTRACT

Burridge (1991) presents an approximate theory of wave propagation of a plane wave through a stack of finely layered and anelastic structure. The theory goes beyond previous works (Burridge and Chang, 1989a & b) in two aspects: (a) the sample autocorrelation rather than the averaged autocorrelation is used so that the coda of the computed response is preserved; (b) anelastic effect due to intrinsic attenuation is incorporated and by "order of magnitude" argument, the terms governing the scattering and anelastic effects enter separately but in a similar way.

The present work is a numerical justification of the approximate theory. Using the *SH* case as an example, we computed the impulse response using two methods: the approximate method and an exact method for an anelastic medium at both normal and oblique incidence. Using a simple standard linear solid model with two relaxation parameters, the medium is made anelastic. Impulse responses obtained by both methods agree well for both elastic and anelastic cases. The results of this preliminary investigation can be summarized in several points: (a) accuracy is best for the head of the pulse; (b) the larger the angle of incidence, the better is the comparison; (c) the presence of anelasticity exhibits the time delay and dispersion of the broad pulse; (d) the broad pulse due to scattering effect is comparable to the pulse due to anelasticity only; (e) the perturbation code is 90 times faster than the exact code for the anelastic case.

INTRODUCTION

The earth varies in many different scales. For plane-stratified subsurface models, it has been shown (O'Doherty and Anstey, 1971; Richards and Menke, 1983; Burridge and Chang, 1989a & b) that the small scale variation can have a significant effect on the amplitude and phase of the transmitted wavefield and can give rise to the apparent attenuation and dispersion. In their previous works, Burridge and Chang (1989a & b) studied the dispersive wave propagation for an impulsive pulse propagating normally or obliquely through a one-dimensional medium consisting of a large number of homogeneous and elastic layers. Immediately following the direct transmitted arrival is a broad pulse. The dispersive effect, in this case, is due to multiply scattered energy. Coda of the pulse was lost because the averaged autocorrelation function was used in the computation. As well, dispersive effect due to intrinsic attenuation is not considered.

In a recent study, Burridge (1991) proposed a method to use the sample autocorrelation function to retain the local details of the reflection series. By this

* open Schlumberger-Doll research report, 1992.

** Schlumberger-Doll Research, CT, USA

means, the coda of the response is preserved. Viscoelastic effects can also be introduced into the same approximate theory though in a more elaborate way than in the ω-k domain. By assuming that the reflection coefficients are small, a small parameter, ε, is introduced to retain relevant terms in the governing equations. It is found that if the reflection coefficients are of order ε and relaxation effect of order ε^2, then they can be separated and have similar overall effects upon the evolution of the pulse. The separation of these two terms allows one to gain a deeper understanding of the similarities and dissimilarities between the effects of anelasticity and of multiple scattering.

The objective of the present work is to implement numerically the approximate solution and to establish accuracy of the approximate method against an exact method. In section II, we will present the approximate expression for a downgoing wave and its implementation for the *SH* case. Incorporation of viscoelastic effect will be illustrated by using a simple staThe earth varies in many different scales. For plane-stratified subsurface models, it has been shown (O'Doherty and Anstey, 1971; Richards and Menke, 1983; Burridge and Chang, 1989a & b) that the small scale variation can have a significant effect on the amplitude and phase of the transmitted wavefield and can give rise to the apparent attenuation and dispersion. In their previous works, Burridge and Chang (1989a & b) studied the dispersive wave propagation for an impulsive pulse propagating normally or obliquely through a one-dimensional medium consisting of a large number of homogeneous and elastic layers. Immediately following the direct transmitted arrival is a broad pulse. The dispersive effect, in this case, is due to multiply scattered energy. Coda of the pulse was lost because the averaged autocorrelation function was used in the computation. As well, dispersive effect due to intrinsic attenuation is not considered.

PERTURBATION METHOD

The problem we want to address is as follows. Figure 1 shows a stack of homogeneous and planar layers, which can be elastic or anelastic, bounded by two half spaces with the same elastic properties. An impulse acts on the first interface at different angle of incidence. We would like to find the *SH* response of the receiver located right beneath the most bottom interface and directly below the point of impact on the first interface. As we want the homogeneous wave to go through the whole layered structure, the ray parameter is restricted to be less than the slowness in any layer. The direct transmitted arrival is not of our interest but close to this arrival is a broad pulse made up of multiply scattered energy (Burridge and Chang, 1989a & b).

The Approximate Solution

Burridge (1991) discussed, in details, the mathematical steps leading to the approximate solutions. Without any repetition, the final expression is quoted. Ignoring the higher order terms, the approximate solution for a downgoing mode is :

$$W(z,.) = e^{[a(z,\theta) + b(z,\theta)]} * W(z=0,.) \qquad (1)$$

where $a(z,\theta)$ represents the effect of *multiple scattering* upon the evolution of the pulse shape and $b(z,\theta)$ represents the effect of *anelasticity*. Note that the operator (*) in

(1).is a convolution operator. The retarded time variable, θ is defined with respect to the direct transmitted arrival. It is worth mentioning the assumption leading to this expression. The crucial point in the theory is the assumption that the variation of reflection coefficients is small *(O(ε))*. If the condition ($R << 1$) is satisfied, then the transmission coefficient ($T = \sqrt{1 - R^2} \approx 1 - \frac{1}{2} R^2 \approx 1$) will have unit value. The structure will be transparent to the wavefield so that at an intermediate step in deriving the solution, the downgoing wavefield $W(z_l, \theta)$ is assumed to be of the same order as $W(z_k, \theta)$ where $z_k \leq z_l$. It is, therefore, expected that there are two conditions that will break down the assumption. Firstly, the reflection coefficients are large. Secondly, even if the coefficient condition is satisfied, the assumption deteriorates with the increase of time for the reflected wavefield from z_l to reach z_k. This can be the case when the wavefield penetrates a deeper part of the structure, i.e., when $(z_l - z_k)$ gets bigger so that the accumulated transmission effect is significant or when the angle of incidence is steep so that it takes longer for the wavefield to reach the receiver. The assumption that the imperfection of elasticity is of 2nd order (smaller than the reflectivity effect) is usually true physically and will be assumed in what follows.

Standard Linear Solid Model

Before we discuss the numerical implementation of equation (1), it is appropriate at this point to choose an anelastic model. The model we used is a primitive standard linear solid (SLS) model which, mechanically can be represented by two springs and a Newtonian dashpot as shown in Figure 2. The dashpot consists of a piston moving in an ideally viscous liquid of viscosity η and its velocity is proportional to the applied force thus providing internal friction by dissipating work done on it as heat (Nowick and Berry, 1972). The behavior of this model is governed by the stress-strain relation (Nowick and Berry, 1972; Aki and Richards, 1980):

$$\sigma + \tau_\sigma \dot{\sigma} = M_r (\varepsilon + \tau_\varepsilon \dot{\varepsilon}) \tag{2}$$

where σ and ε are stress and strain, M_r is the relaxed modulus, τ_σ is the relaxation time due to constant strain, τ_ε is the relaxation time due to constant stress and the dot signifies the time derivative.

For a step load, the strain response is

$$\varepsilon(t) = \frac{1}{M_r}\left[1 - \left(1 - \frac{\tau_\sigma}{\tau_\varepsilon}\right) \exp\left(-\frac{t}{\tau_\varepsilon}\right)\right] H(t) \quad . \tag{3}$$

Note that

$$\varepsilon(t = +0) = \frac{\tau_\sigma}{M_r \tau_\varepsilon} = \frac{1}{M_u} = J_u \tag{4}$$

and

$$\underset{(t \rightarrow \infty)}{\varepsilon} \rightarrow \frac{1}{M_r} = J_r \tag{5}$$

where M_u , J_u and J_r are the unrelaxed modulus, unrelaxed compliance and relaxed compliance. This can be explained as follows. Upon application of a step load at t=0, the spring characterized by J_u deforms immediately according to Hooke's law while the Voigt unit remains undeformed due to the fact that the dashpot resists sudden change. Thus at $t=0$, the strain of the whole system is given by the unrelaxed compliance J_u of the spring [equation (4)]. As time goes by, the dashpot will flow to release the stress upon the Voigt unit. As the stress of the Voigt unit vanishes, the spring of the Voigt unit is deforming toward an equilibrium strain given by the compliance of the spring, ΔJ . Eventually, the strain of the whole system is given by $J_u + \Delta J = J_r$ of the two springs in accordance with equation (5).

For an impulsive load $\sigma(t) = \delta(t)$, we differentiate (3) to obtain

$$\dot{\varepsilon}(t) = \frac{1}{M_u}\,\delta(t) + \frac{1}{M_u}\left(\frac{1}{\tau_\sigma} - \frac{1}{\tau_\varepsilon}\right)\exp\left(-\frac{t}{\tau_\varepsilon}\right)H(t) \tag{6}$$

where we have used the relation

$$M_r = M_u\,\frac{\tau_\sigma}{\tau_\varepsilon} \quad . \tag{7}$$

Similarly, for a step strain, $\varepsilon(t) = H(t)$ the stress response is

$$\sigma(t) = M_r\left[1 - \left(1 - \frac{\tau_\varepsilon}{\tau_\sigma}\right)\exp\left(-\frac{t}{\tau_\sigma}\right)\right]H(t) \tag{8}$$

and for an impulsive strain $\varepsilon(t) = \delta(t)$,

$$\dot{\sigma}(t) = M_u\,\delta(t) + M_u\left(\frac{1}{\tau_\varepsilon} - \frac{1}{\tau_\sigma}\right)\exp\left(-\frac{t}{\tau_\sigma}\right)H(t) \quad . \tag{9}$$

The right hand side of equation (6) [or equation (9)] expresses the total compliance (or modulus) of the three-element SLS model.

In terms of frequency, the phase velocity is given by

$$[c(\omega)]^2 = \frac{M(\omega)}{\rho} \tag{10}$$

and the internal friction by

$$\frac{1}{Q(\omega)} = -\frac{\mathrm{Im}M(\omega)}{\mathrm{Re}M(\omega)} = \frac{(\tau_\varepsilon - \tau_\sigma)\omega}{\omega^2\tau_\varepsilon\tau_\sigma + 1} \tag{11}$$

where

$$M(\omega) = \frac{M_u}{1 + \left(\frac{\tau_\varepsilon}{\tau_\sigma} - 1\right)(1 + i\omega\tau_\varepsilon)\,(1 + \omega^2\tau_\varepsilon^2)^{-1}} \quad . \tag{12}$$

We note that

$$M(\omega \to 0) = M_r \tag{13}$$

and

$$\underset{(\omega \to \infty)}{M} \to M_u \tag{14}$$

By comparing (13) – (14) with (4) – (5), we find the low frequency behavior corresponds to the long time anelastic effect and the high frequency behavior to the instantaneous elastic response. This can be predicted from (2). Since the derivative in time goes into multiplication by frequency via Fourier transform, at low frequency the contribution from the derivative terms is negligible and the relaxed modulus governs the behavior. At high frequency, the opposite is true. The non-derivative terms drop and the unrelaxed modulus takes control of the system. Figures 3 and 4 show a plot of the internal friction $[Q(\omega)]^{-1}$ and the square of phase velocity $[c(\omega)]^2$ with frequency for $\tau_\varepsilon = 2.5\text{E-}4$ and $\tau_\sigma = 2.4\text{E-}4$.

Numerical Implementation

In a piecewise homogeneous medium, the scattering argument of the exponential convolution operator is

$$a(z,\theta) = \sum_{\substack{k,l \\ \text{where } k \le l}} \sigma_{kl}\, R_{12}^{(l)}\, R_{21}^{(k)}\, \delta(\theta - \hat{\tau}(z_k, z_l)) \tag{15}$$

where $R_{12}^{(l)}\left(R_{12}^{(l)} = -R_{21}^{(l)}\right)$ is the normalized SH reflection coefficient (Figure 5) of the l'th interface, $\hat{\tau}(z_k, z_l)$ is the two-way travel time between z_k and z_l and

$$\sigma_{kl} = \begin{cases} \frac{1}{2} \ , & \text{if } k = l \\ 1 \ , & \text{otherwise} \end{cases} . \tag{16}$$

In practice, we would like to calculate a discrete form of $a(z,\theta)$. Thus, we discretize the variable θ, dividing its range into intervals $\left[(m-\frac{1}{2})h\ ,\ (m+\frac{1}{2})h\right]$, where m takes on integer values and h is the step size. We then accumulate a discrete form of the quantity $a(z,\theta)d\theta$ as follows: Fix the receiver position z. Set $a_m(z) = 0$ for all relevant integer m. Then, for each admissible pair $k \neq l$ find m such that

$$(m-\tfrac{1}{2})h \le \hat{\tau}_j(z_k,z_l) \le (m+\tfrac{1}{2})h \tag{17}$$

and add to $a_m(z)$ the quantity

$$-R_{12}^{(l)}\, R_{12}^{(k)} \tag{18}$$

If $k=l$, we add to $a_0(z)$ the contribution

$$-\frac{1}{2}\left(R_{12}^{(l)}\right)^2 \tag{19}$$

where we have used the approximation

$$T_{12}^{(l)} = \sqrt{1-\left(R_{12}^{(l)}\right)^2} \approx 1-\frac{1}{2}\left(R_{12}^{(l)}\right)^2 \tag{20}$$

and $T_{12}^{(l)}$ is the normalized transmission coefficient of the l'th interface. The one-dimensional array $a_m(z)$ is now a discretized form of $a(z,\theta)d\theta$.

The effect of attenuation is accounted for by the anelastic argument:

$$b(z,\theta) = -\sum_{i=1}^{N-1}\left(e_i^T J\, \partial_t M_i^{(1)} e_i\right)\Delta z_i \tag{21}$$

where the superscript T denotes the transpose of a vector, z_i is the thickness of the i'th layer,

$$J = \begin{bmatrix} 0 & 1 \\ 1 & 0 \end{bmatrix}, \tag{22}$$

and e is the normalized eigenvector of the SH system (27) discussed below:

$$e = C\begin{pmatrix} \frac{1}{\mu} \\ \\ \gamma \end{pmatrix} \tag{23}$$

where C is the normalized factor with respect to the energy flux

$$C = \sqrt{\frac{\mu}{2\gamma}} \tag{24}$$

and

$$\gamma = \sqrt{\frac{1}{\mu}(\rho - p^2\mu)} \quad . \tag{25}$$

The matrix $M_i^{(1)}$ in (21) is the anelastic part of the stiffness matrix, M :

$$y_z = M\, y_t, \tag{26}$$

where y is the z-component of the displacement-stress vector and

$$M = \begin{bmatrix} 0 & \frac{1}{\mu} \\ \\ \rho - p^2\mu & 0 \end{bmatrix} . \tag{27}$$

Using the compliance (6) and modulus (9) of the SLS model, we split up the stiffness matrix into two parts: elastic part $M^{(0)}$ and anelastic part $M^{(1)}$:

$$M = M^{(0)} + M^{(1)}, \tag{28}$$

where

$$M^{(0)} = \begin{bmatrix} 0 & \frac{1}{\mu_u} \\ \rho - p^2\mu_u & 0 \end{bmatrix} \tag{29}$$

and

$$M^{(1)} = \begin{bmatrix} 0 & \frac{1}{\mu_u}\left(\frac{1}{\tau_\sigma} - \frac{1}{\tau_\varepsilon}\right) \exp\left(-\frac{t}{\tau_\varepsilon}\right) H(t) \\ p^2\mu_u\left(\frac{1}{\tau_\sigma} - \frac{1}{\tau_\varepsilon}\right) \exp\left(-\frac{t}{\tau_\sigma}\right) H(t) & 0 \end{bmatrix}. \tag{30}$$

Thus,

$$\partial_t M^{(1)} = \begin{bmatrix} 0 & \frac{1}{\mu_u}\left(\frac{1}{\tau_\sigma} - \frac{1}{\tau_\varepsilon}\right)\left\{\delta(t) - \frac{1}{\tau_\varepsilon}\exp\left(-\frac{t}{\tau_\varepsilon}\right) H(t)\right\} \\ p^2\mu_u\left(\frac{1}{\tau_\sigma} - \frac{1}{\tau_\varepsilon}\right)\left\{\delta(t) - \frac{1}{\tau_\sigma}\exp\left(-\frac{t}{\tau_\sigma}\right) H(t)\right\} & 0 \end{bmatrix}. \tag{31}$$

The discrete form of $b(z,\theta)d\theta$ is somewhat easier to calculate than the discrete form of $a(z,\theta)d\theta$. For each $\theta = mh$ where $m = 0,1,2,...$ is the time index, we calculate the discrete sum

$$b_m(z) = b(z,\theta)d\theta \tag{32}$$

and assign the cumulated sum to the bin of index m. Thus when $m = 0$,

$$b_0 = -\sum_{i=1}^{N-1} C_i \left\{\rho_i - p^2\mu_i\left[1 - \exp\left(-\frac{h}{2(\tau_\sigma)_i}\right)\right] - (\rho_i - p^2\mu_i)\left[1 - \exp\left(-\frac{h}{2(\tau_\varepsilon)_i}\right)\right]\right\} \Delta z_i \tag{33}$$

and when $m > 0$,

$$b_m = -\sum_{i=1}^{N-1} C_i \left\{\rho_i - 2\,p^2\mu_i \exp\left(-\frac{m\,h}{(\tau_\sigma)_i}\right) \sinh\left(\frac{h}{2(\tau_\sigma)_i}\right)\right.$$
$$\left. -2\,(\rho_i - p^2\mu_i) \exp\left(-\frac{m\,h}{(\tau_\varepsilon)_i}\right) \sinh\left(\frac{h}{2(\tau_\varepsilon)_i}\right)\right\} \Delta z_i \tag{34}$$

where

$$C = \frac{1}{2} \frac{\left(\frac{1}{\tau_\sigma} - \frac{1}{\tau_\varepsilon}\right)}{\sqrt{\mu(\rho - \mu p^2)}} \quad . \tag{35}$$

We now take the discrete convolutional exponential of $a_m(z) + b_m(z)$ in the discrete time domain. Let us set

$$c_m(z) = a_m(z) + b_m(z) \tag{36}$$

Assuming the function $a(z,\theta)$ is causal in θ, we define the generating function

$$C(\xi) = \sum_{m \geq 0} c_m \, \xi^m \quad . \tag{37}$$

If u_m is the convolutional exponential of c_m, we have

$$U(\xi) = \sum_{m \geq 0} u_m \, \xi^m = e^{[C(\xi)]} \, . \tag{38}$$

Now differentiate with respect to ξ to get

$$\frac{d\,U(\xi)}{d\xi} = U(\xi) \frac{d\,C(\xi)}{d\xi} \tag{39}$$

On equating the coefficient of various powers of ξ on the two sides of the equation and dividing by m we obtain

$$u_m = \frac{1}{m} \sum_{p=1}^{m} p \, c_p \, u_{m-p} \tag{40}$$

Since the right member of (40) contains only $u_0,\ldots,u_{m-1}$, this formula may be used to calculate the u_m recursively.

EXACT SIMULATION USING FREQUENCY-SLOWNESS (ω-p) METHOD

Given a spectrum of frequencies up to a Nyquist frequency, the simulation code calculates the exact impulse response, via inverse FFT, by calculating the global reflection and transmission coefficients of the entire multi-layered structure. The algorithm used in this work was briefly described by Chang (1987) and requires computation of ordinary reflection and transmission coefficients for an interface. The recursive relation for the global reflection coefficient, R_n is

$$R_n = R^{n,n+1} + T^{n+1,n} P^{(2)}_{n+1} R_{n+1} (I - P^{(1)}_{n+1} R^{n+1,n} P^{(2)}_{n+1} R_{n+1})^{-1} P^{(1)}_{n+1} T^{n,n+1} \quad (41)$$

and the global transmission coefficient, T_n is

$$T_n = T_{n+1} (I - P^{(1)}_{n+1} R^{n+1,n} P^{(2)}_{n+1} R_{n+1})^{-1} P^{(1)}_{n+1} T^{n,n+1} \quad (42)$$

for $n = N\text{-}1,...,1$ where N is the number of layers and I is the identity matrix. $R^{i,j}$ and $T^{i,j}$ are the ordinary reflection and transmission coefficients normalized by the energy flux for two half-spaces and $P^{(1)}_{n+1}$ and $P^{(2)}_{n+1}$ are the exponentials whose arguments are the vertical phase factors. The global or local reflection and transmission coefficients, R and T are 2 x 2 matrices for the *P-SV* case and scalar for the *SH* case.

The computation procedure is to start the recursion at the bottom interface with the initial values:

$$R_{N-1} = R^{N-1,N} \quad (43)$$

and

$$T_{N-1} = T^{N-1,N} \quad (44)$$

and work upward to the top layer.

DISCUSSION OF THE NUMERICAL RESULTS

The synthetic model we used was generated and made available to us by Kai Hsu. It consists of 1750 homogeneous isotropic layers bounded between two half-spaces having the same elastic properties. Figures 6 - 8 show the model in metric scale. Velocities were randomly generated and uniformly distributed with means 50 μs/ft, 67 μs/ft and 33 μs/ft respectively and standard deviations 15 μs/ft, 20 μs/ft and 10 μs/ft respectively to make up three distinct zones. Constant density of 2.5 gm/cc is used for all layers. The thickness sequence is generated by the exponential thickness model with means 2 ft, 1 ft and 4 ft. Figures 9 and 10 show the individual one-way travel time and accumulated one-way travel time at normal incidence. Reflection and transmission coefficients against depth are displayed in Figures 11 and 12. The coefficients are normalized by the energy flux so that the sum of the squared transmission and squared reflection coefficients is unity. As seen from the figures, the model has a wide range of coefficient values. One might speculate that this kind of coefficient variation would violate the assumption mentioned in section 2.1, thus degrading the approximate result. Surprisingly, the comparison is very good for the early arrival. Figure 13 shows the scattering bin, a_m or autocorrelation "function" at normal incidence. The bin values can be best fitted by an exponential curve which has a sharp and large positive value, to start with, becomes negative and then tapers asymptotically to zero. Figure 14 shows the cumulated scattering bin. From the expression characterizing the anelastic effect, one would expect the same exponential behavior for b_m. Figure 15 plots 50 points from the scattering bin, anelastic bin and the sum of both.

Figure 16 shows the sensitivity of the exact results to different Nyquist frequencies and sampling rates. The effect of increasing the sampling points on the coda amplitude is greater at high Nyquist frequency (10 KHz) than at low frequency (2.5 KHz) (compare Figure 16(A) with (B); Figure 16(C) with (D) or see Figure 17). Increasing the Nyquist frequency at fixed sampling rate does not seem to change the general character of the result as shown in Figure 18. However, because the time step is smaller, detailed resolution is enhanced, thus making the trace look rougher. Figure 19 shows the sensitivity of the approximate solution to different time steps. A larger time step increases the smoothing effect since more values [a_m or b_m or both] are added into the same bin [Figure 19(A)]. Using too small a time step, on the other hand, conveys more details than necessary [Figure 19(D)]. Bearing these two limitations in mind we chose to calculate approximate results using a time step 0.5E-4 and exact results using 4096 points and $f_{Nyquist}$ = 2.5 KHz.

Elastic Comparison

Figures 20-24 shows the comparison between the approximate and exact elastic results at 5 different angles of incidence (0^0, 5^0, 10^0, 15^0, 20^0). The exact solutions are solid curves and the approximate solutions are dotted. Accuracy is best for the head of the pulse and deteriorates as time increases. This is well predicted from the assumption made in the theory. Discrepancy between approximate and exact results decreases as the angle of incidence increases. Because the receiver is directly below the impact point, the wavefield will reach the receiver sooner at larger angle of incidence. Amplitude increases with angle of incidence as well. In all cases, the approximate coda advances the exact coda in time. Figure 25 puts all five figures (Figures 20-24) together. The computation was done in the Cray X-MPEA and took 1.2 sec for the approximate result and 21 sec for the exact result.

Anelastic Comparison

Anelastic comparisons are shown in Figures 26-30. Time delay and dispersion effect are obvious. The discrepancy in this case can be explained by the same argument as in the elastic case. By comparing Figure 30 with Figure 24, it is tempting to conclude that the anelastic solution is more stable than the elastic one. This is true since anelasticity smooths the "roughness" of the spectrum, thus giving rise to a smoother response. Figure 31 plots all five figures (Figures 26-30) together. The computing time for the anelastic case was 5 sec for the approximate result and 7.5 min for the exact result. The cumulative sum of the elastic and anelastic responses are given in Figure 32, providing another means of comparing results calculated by two different methods. Note that the cumulative quantity here has nothing to do with energy. It simply means that the area is conserved, i.e. an impulse of unit area was injected into the medium and the sum of output should approach one as well. Figure 33 shows the impulse response for the dissipative effect only. The results should not change very much with different angles of incidence since the exponential terms in (33-34) decay rapidly with time (due to the large values of the relaxation constants). The dissipative pulse is comparable to the broad pulse due to scattering effect alone (compare Figure 25 with Figure 33).

CONCLUSION

In this paper, we have numerically justified the accuracy of the approximate methods by using the *SH* case as an example. The accuracy is best for the broad pulse

immediately after the direct transmitted arrival. For all five angles of incidence considered, the approximate coda is ahead of the exact coda in time. However, the approximate code is significantly faster than the exact code.

The work reported here cannot be claimed to be completed since the comparison was done for one model case only. Studies of the *P-SV* case and of the sensitivity of the approximate results to different layer thickness, source spectrum and, most importantly, different reflectivity sequences have not been thoroughly done but are in progress. Such a study will establish the domain of validity of the approximate theory, thus providing a powerful means of understanding the effects of multiple scattering and anelasticity on seismic wave.

ACKNOWLEDGEMENT

We thank Andrew Norris, Kai Hsu, and Martijn de Hoop for very helpful discussions, Hung Wen Chang at SLCS for his hospitality and technical assistance, and for his continued advice on modifying the simulation program. We thank Ray Kocian, Karyn Muller and Sergio Kostek for their assistance in various aspects of using the Vax, Cray and Matlab, the GEO and EMG groups, especially Chung Chang, Yupai Hsu and Chaur-Jian Hsu for creating a warm atmosphere, and Kai Hsu for providing the synthetic model.

REFERENCES

K. Aki and Richards, P.G. ,1980, Quantitative Seismology: Theory and Methods: Volume 1, W.H. Freeman and Company.

R. Burridge, 1991, Waves in finely layered and anelastic media:, private communication.

R. Burridge and Chang, H.W., 1989a, Multimode, one-dimensional wave propagation in a highly discontinuous medium: Wave Motion 11, 231-249.

R. Burridge and Chang, H.W., 1989b, Pulse evolution in a multimode, one-dimensional, highly discontinuous medium: in Elastic wave propagation edited by M.F. McCarthy and M.A. Hayes, Elsevier, 229-234.

Chang, H.W., 1987, 3-D reflection/transmission coefficients from cylindrical layered elastic media: Ultrasonics symposium, 455-459.

A.S. Nowick and Berry, B.S., 1972, Anelastic Relaxation in Crystalline Solids: chapter 3, Academic Press.

R.F. O'Doherty and Anstey, N.A.. 1971, Reflections on amplitudes: Geophys. Prosp. 19, 430-458.

P.G. Richards and Menke, W., 1983, The apparent attenuation of a scattering medium: Bull. Seism. Soc. Amer. 73, 1005-1021.

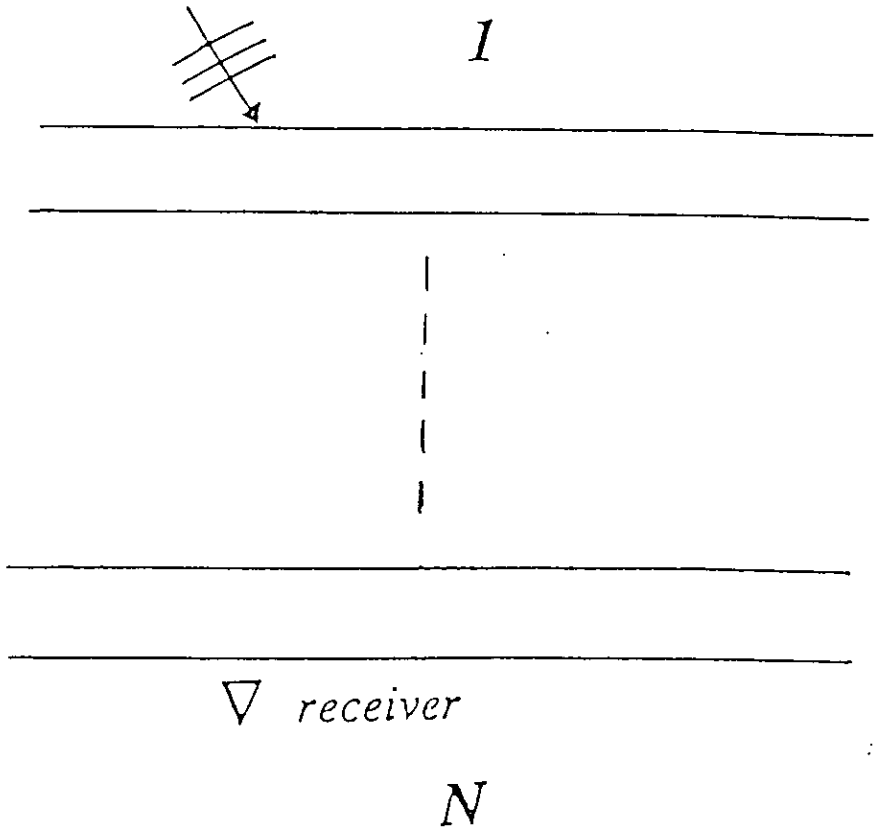

Figure 1 : A model consists of *N-2* layers bounded by two half spaces.

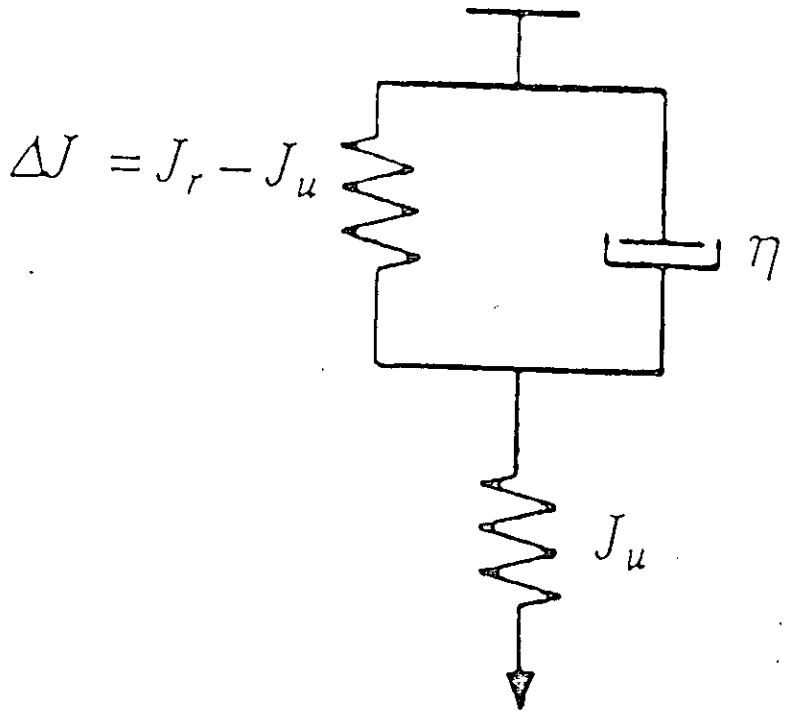

Figure 2 : An example of a three-element standard linear solid model: a Voigt unit in series with a spring (from Nowick and Berry, 1972).

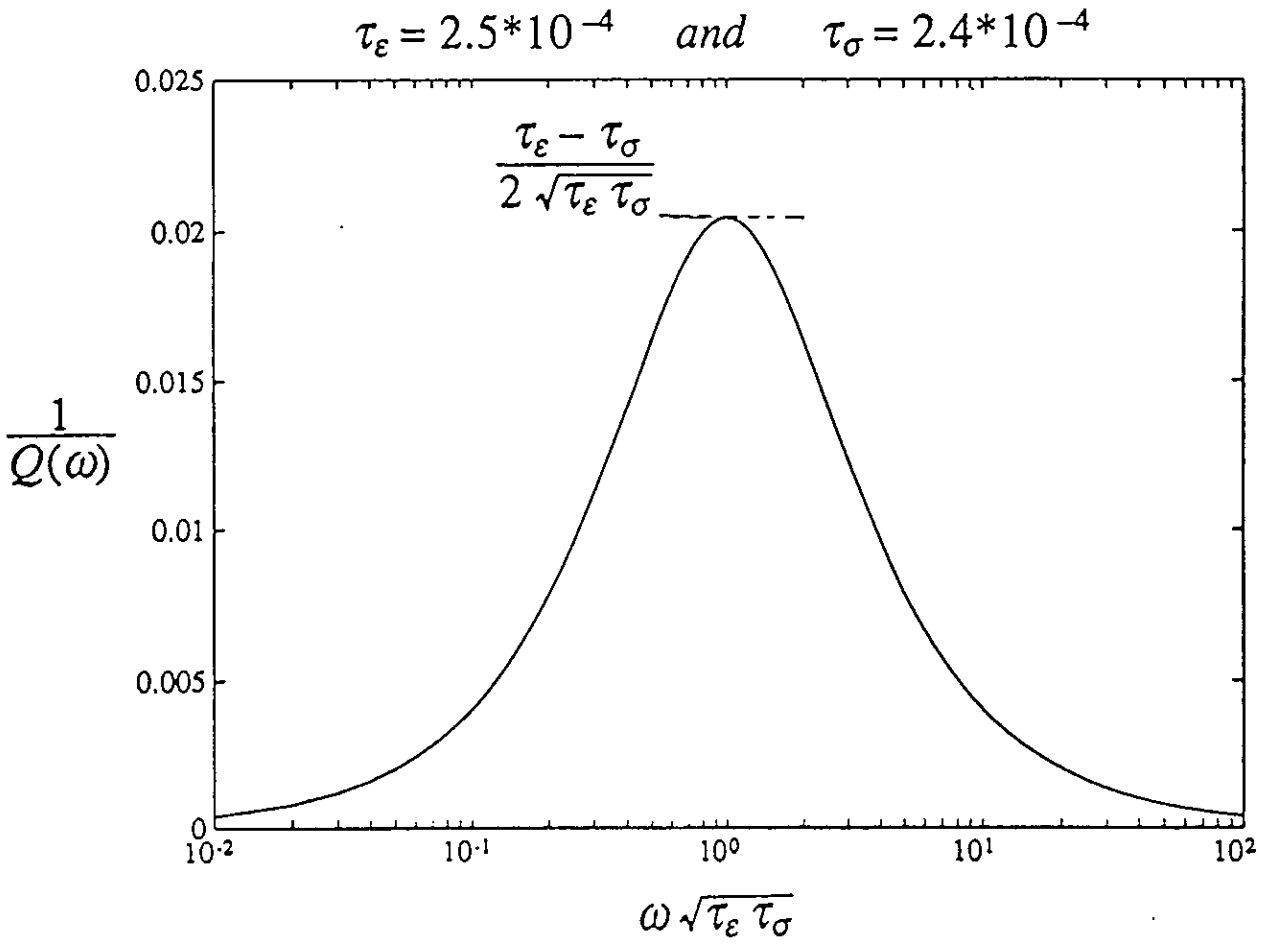

Figure 3 : The internal friction Q^{-1} as a function of frequency in an SLS with a single relaxation peak.

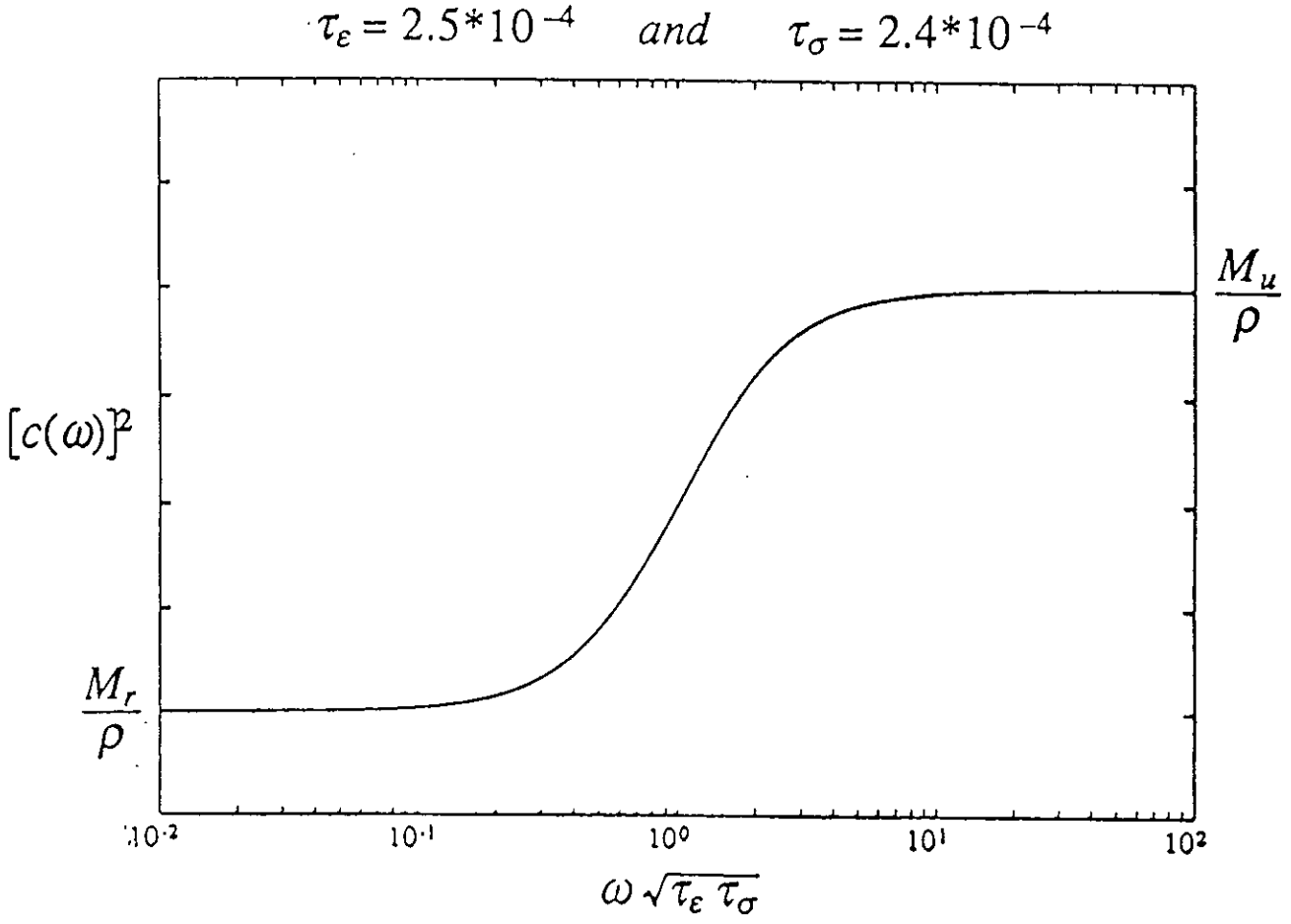

Figure 4 : The square of phase velocity $[c(\omega)]^2$ as a function of frequency in an SLS with a single relaxation peak.

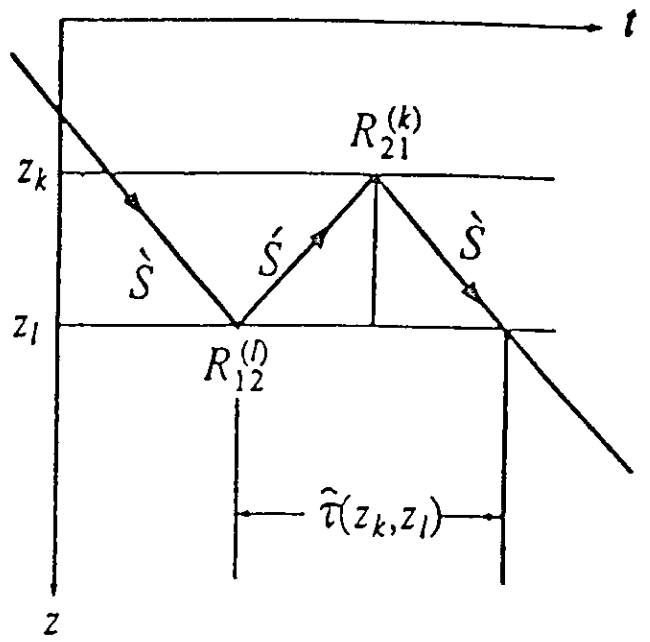

Figure 5 : Time-space diagram showing a double scattering.

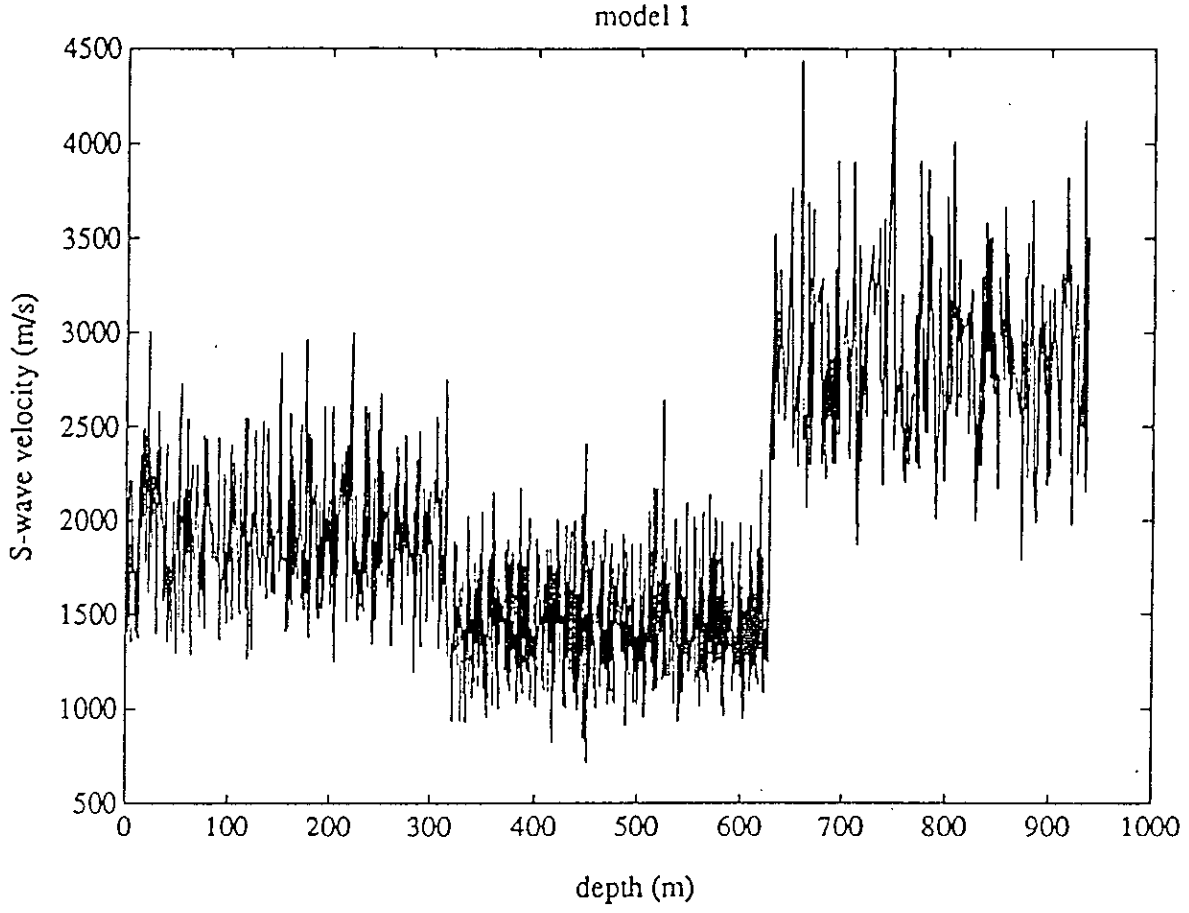

Figure 6 : Synthetic *SH* velocity log containing 1750 layers bounded between two half-spaces with the same elastic properties. Velocities are randomly generated and uniformly distributed. The means are 50 μs/ft, 67 μs/ft and 33 μs/ft and the standard deviations are 15 μs/ft, 20 μs/ft and 10 μs/ft respectively.

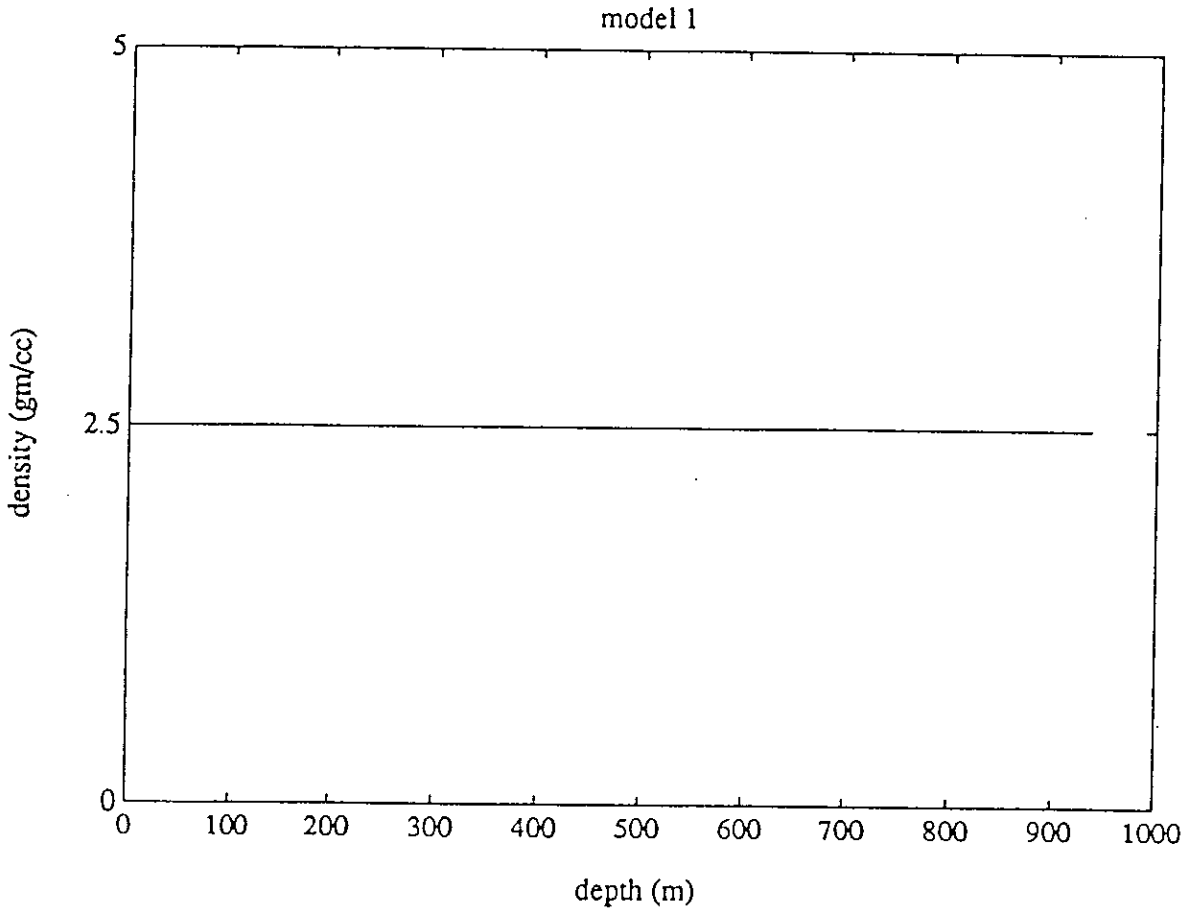

Figure 7 : Constant density log for all layers.

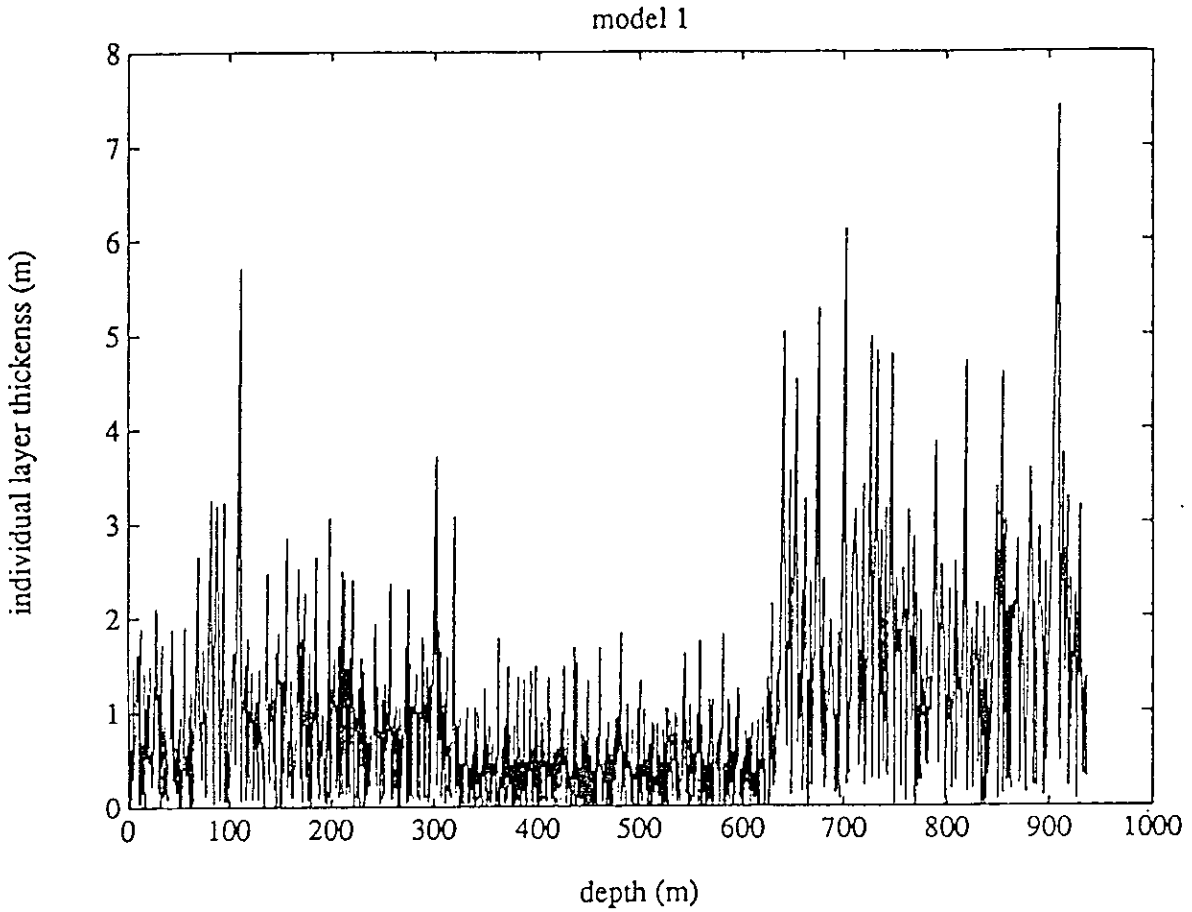

Figure 8 : Synthetic thickness log for 1750 layers. The first and last layers have zero thickness representing the half-spaces. Thickness are exponentially distributed with means 2 ft, 1 ft and 4 ft respectively.

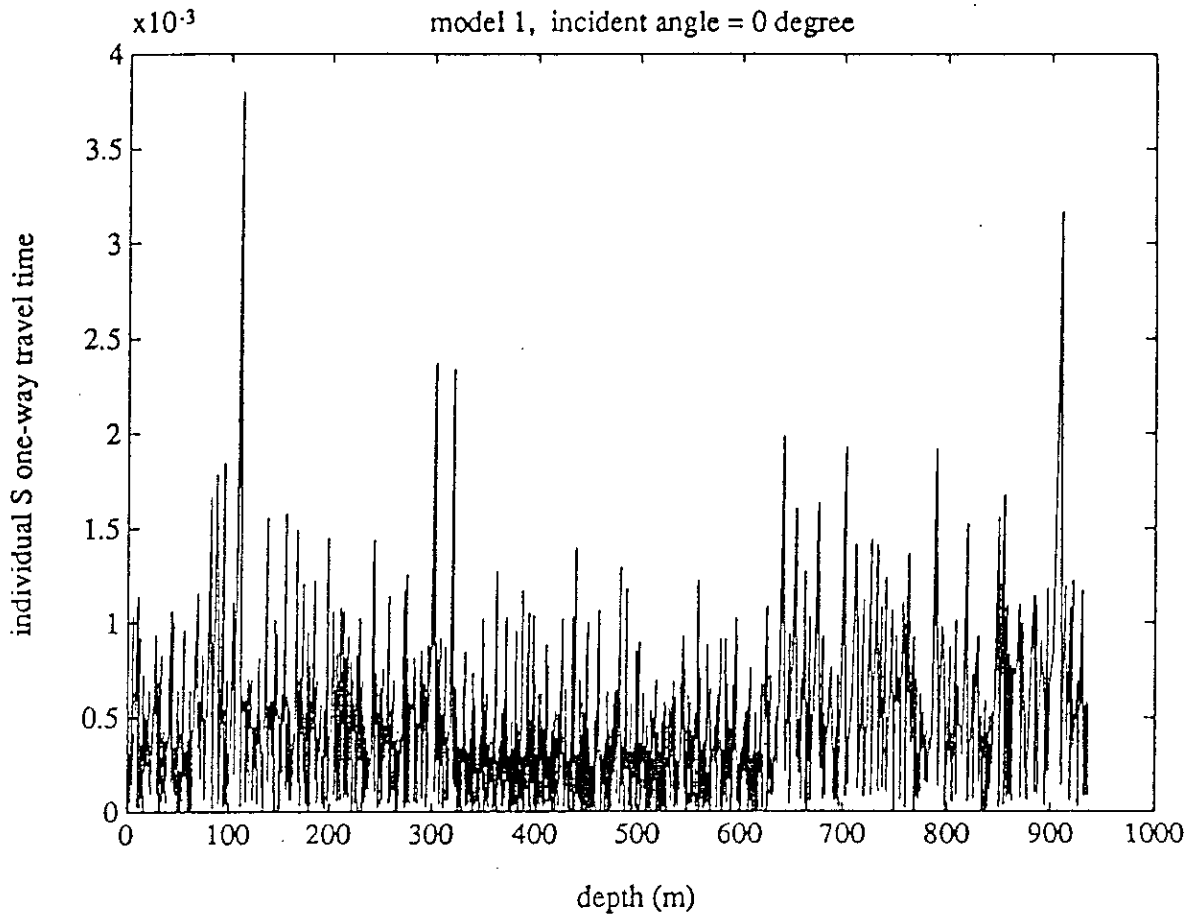

Figure 9 : Distribution of calculated one-way travel time within each individual layer at normal incidence.

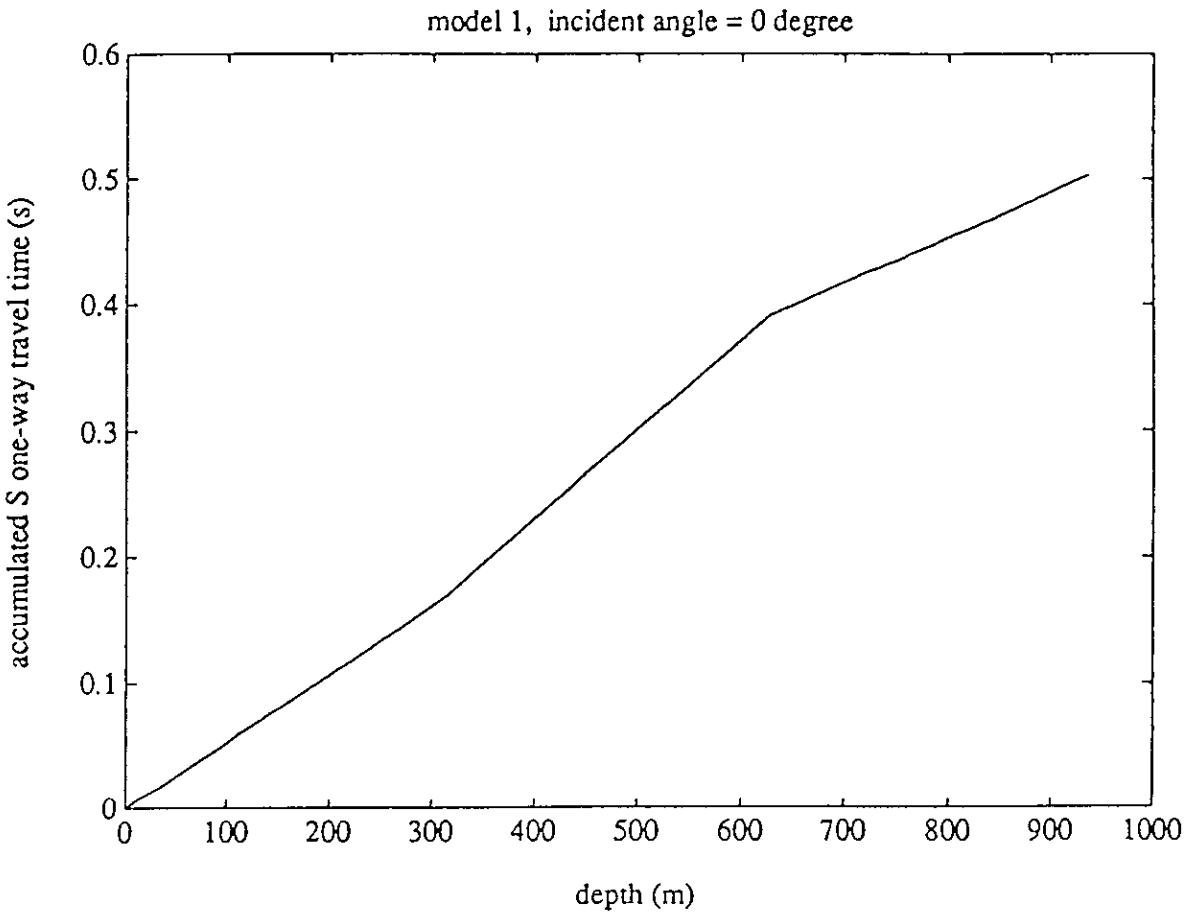

Figure 10 : Accumulated one-way travel time at normal incidence.

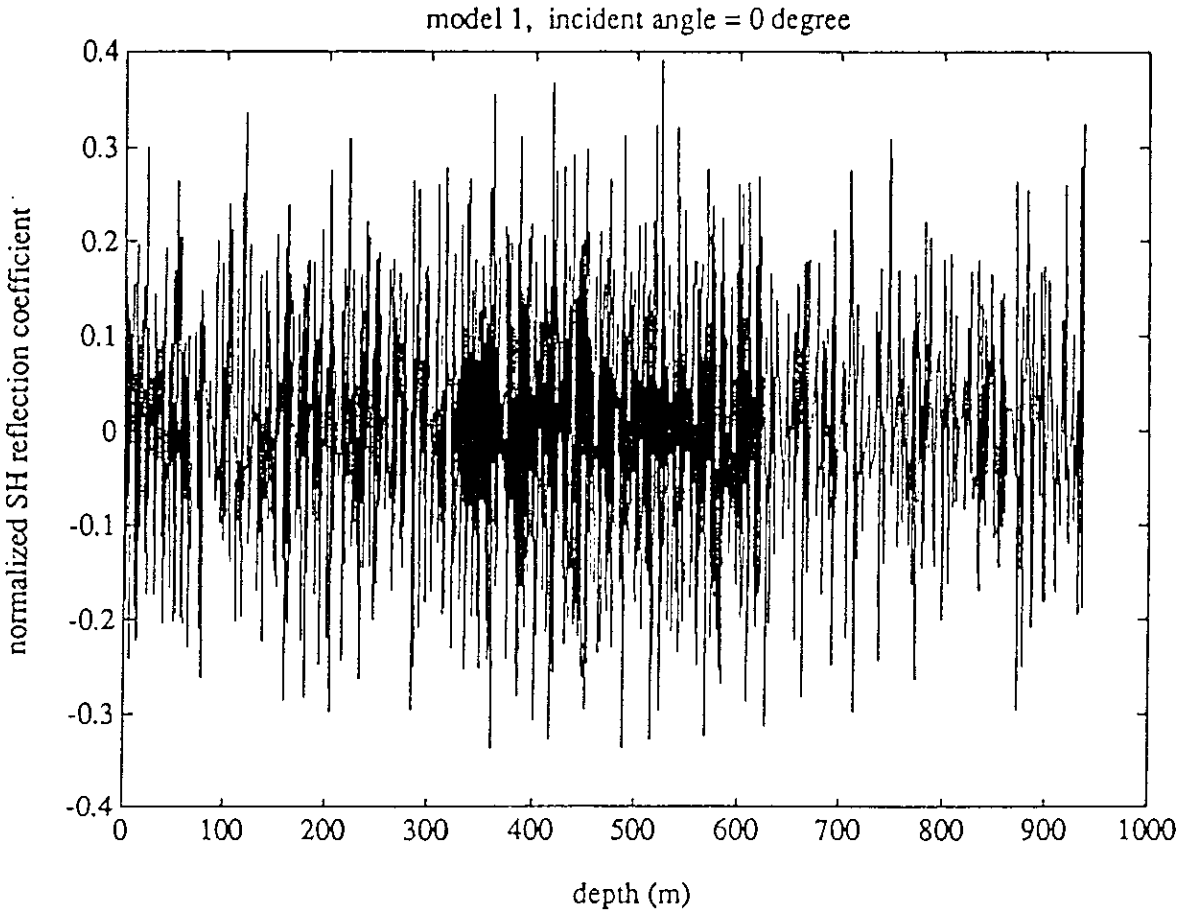

Figure 11 : Distribution of normalized *SH* reflection coefficient at normal incidence.

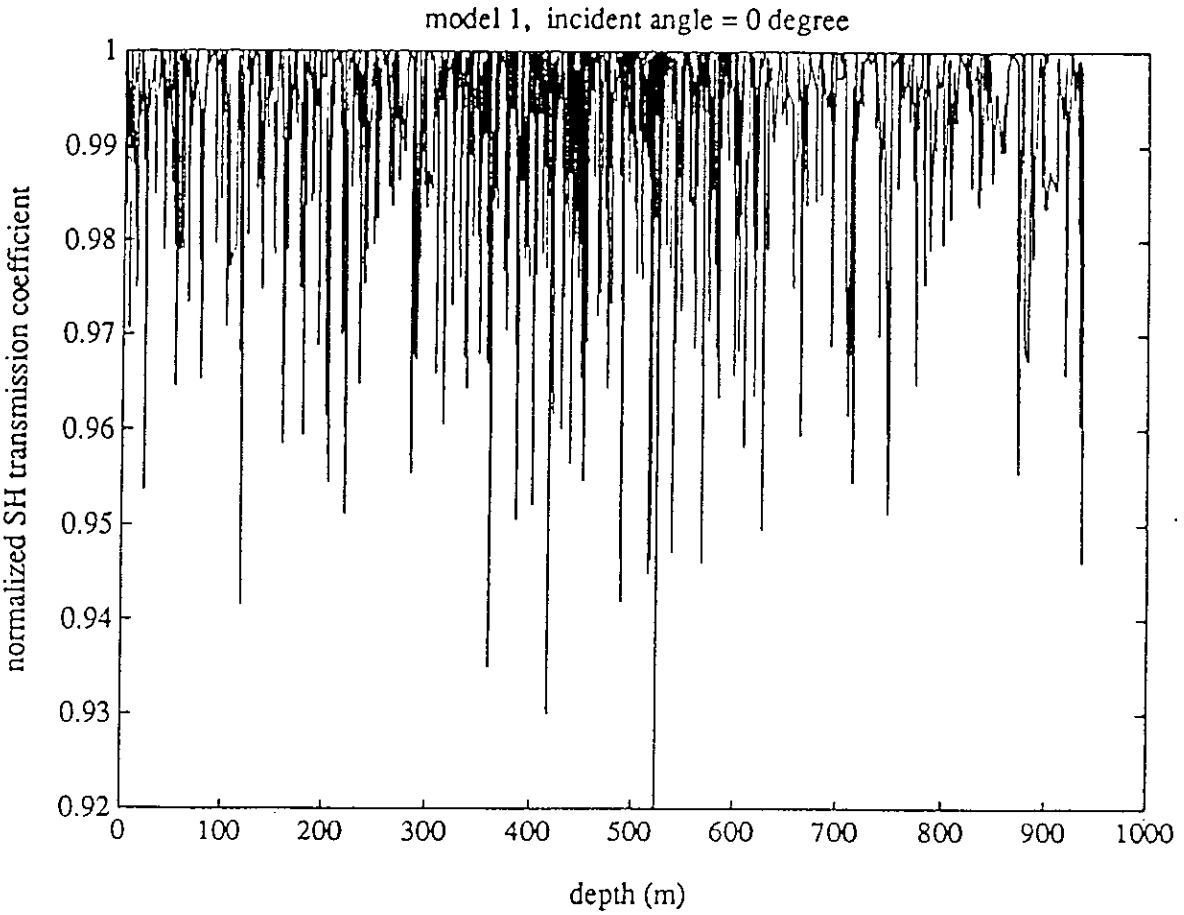

Figure 12 : Distribution of normalized *SH* transmission coefficient at normal incidence.

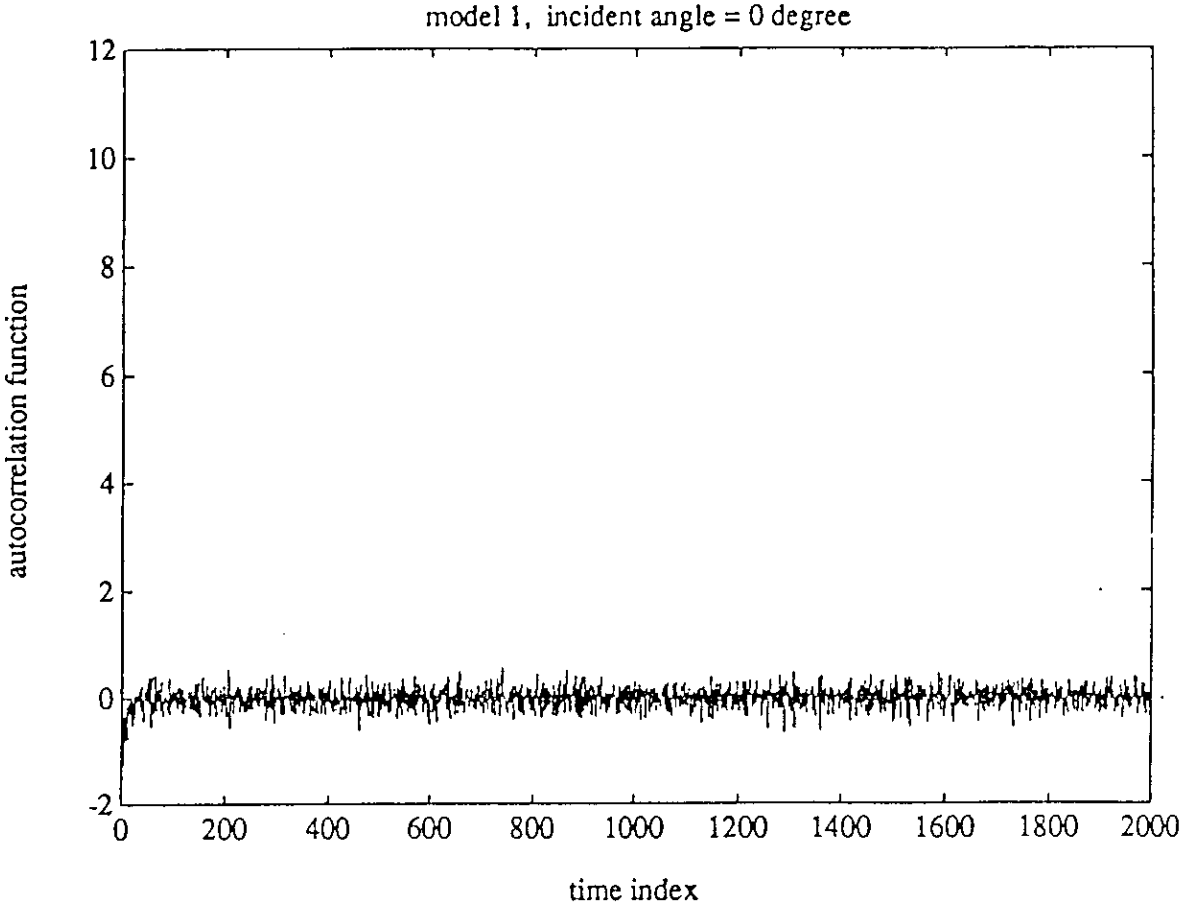

Figure 13 : Scattering bin at normal incidence.

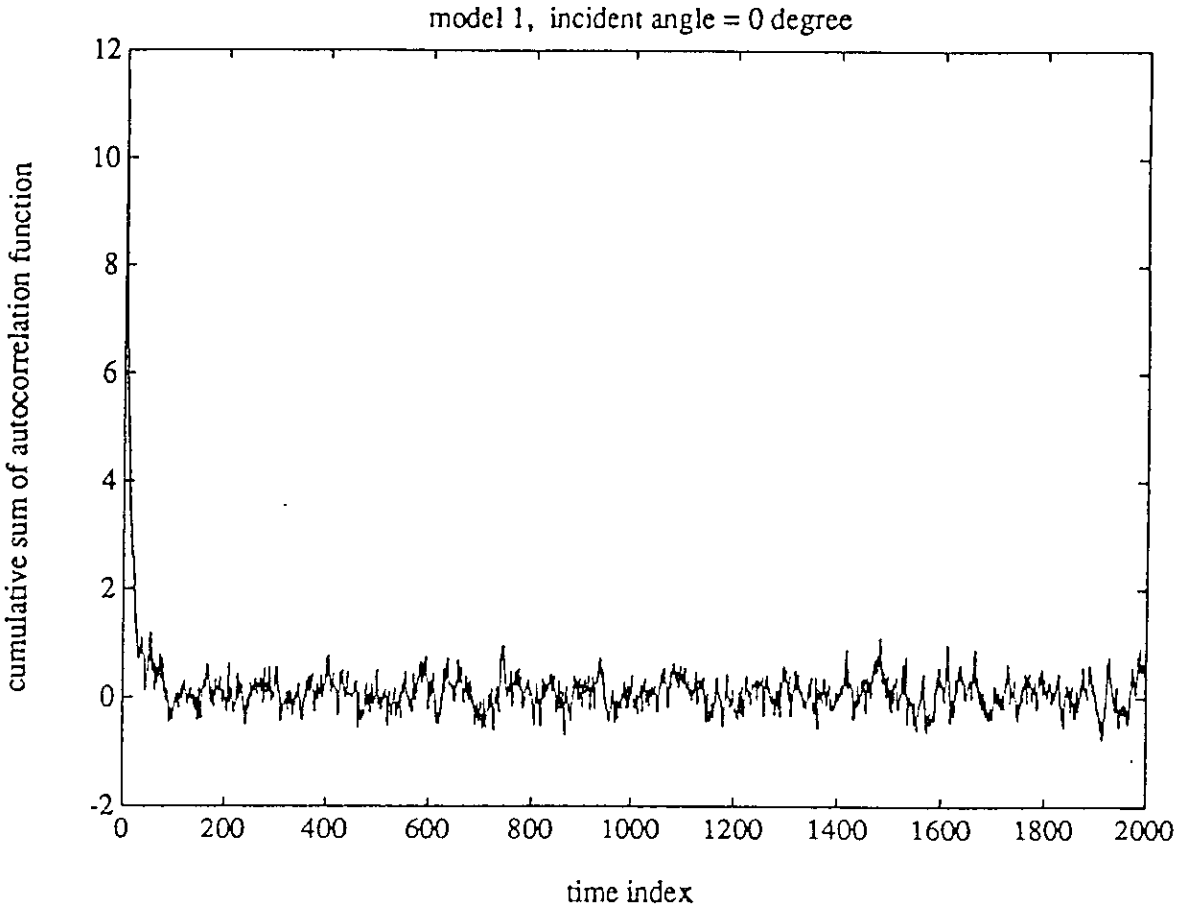

Figure 14 : Cumulative sum of scattering bin at normal incidence.

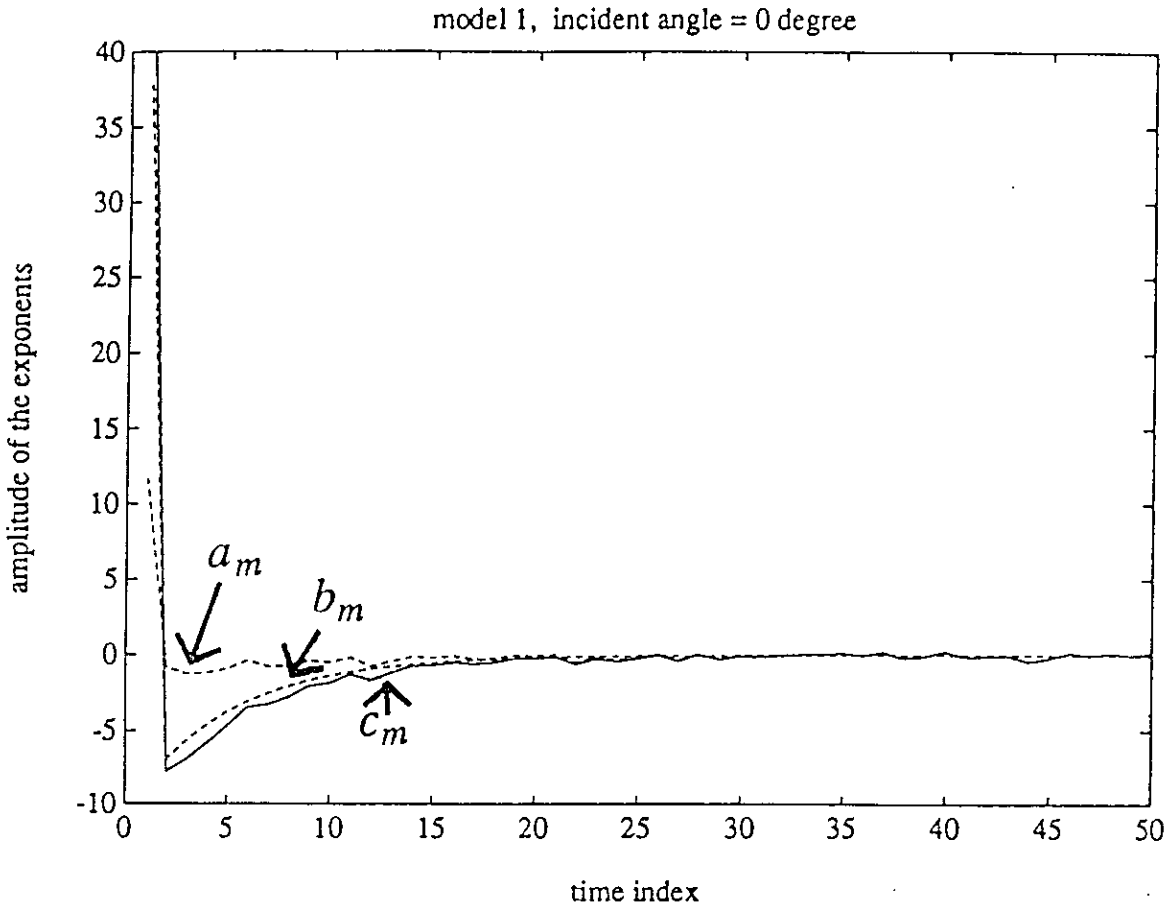

Figure 15 : Scattering bin (dashed), anelastic bin (dashed) and the sum of both (solid).

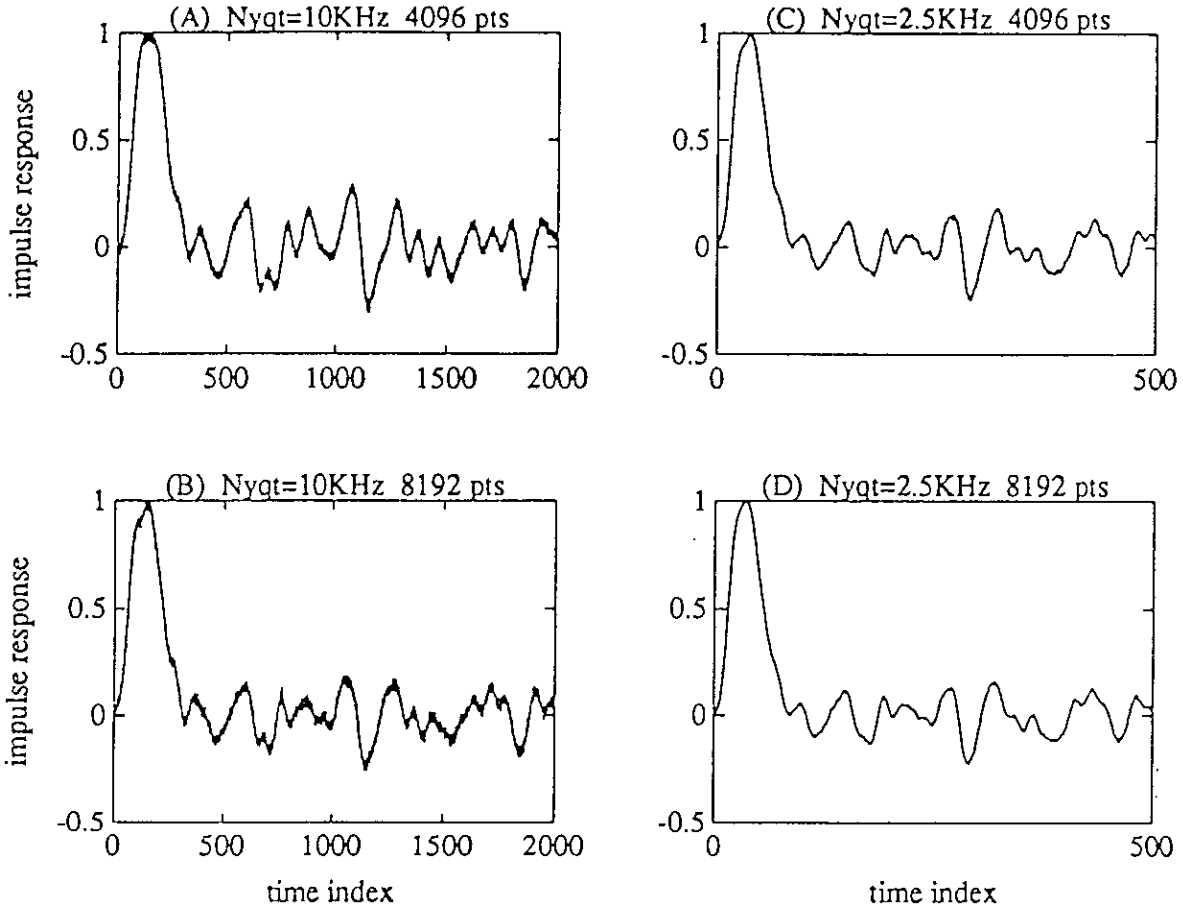

Figure 16 : Comparison of elastic impulse responses calculated by exact method using different frequency parameters : (A) $f_{Nyquist}$ = 10 KHz with 4096 points; (B) $f_{Nyquist}$ = 10 KHz with 8192 points; (C) $f_{Nyquist}$ = 2.5 KHz with 4096 points; (D) $f_{Nyquist}$ = 2.5 KHz with 8192 points.

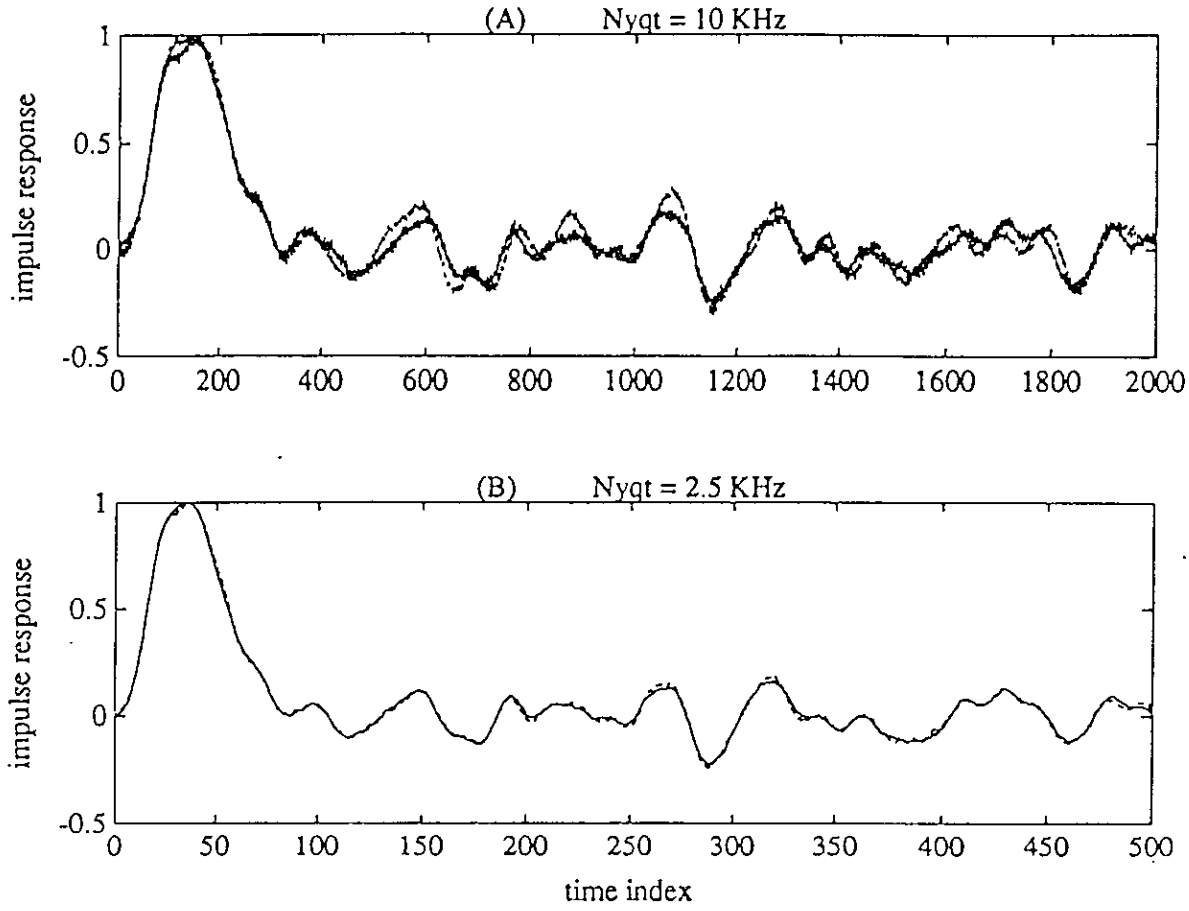

Figure 17 : Comparison of elastic impulse responses calculated by exact method using two different sampling rates : (A) $f_{Nyquist}$ = 10 KHz and (B) $f_{Nyquist}$ = 2.5 KHz (Solid : 8192 points; dashed : 4096 points).

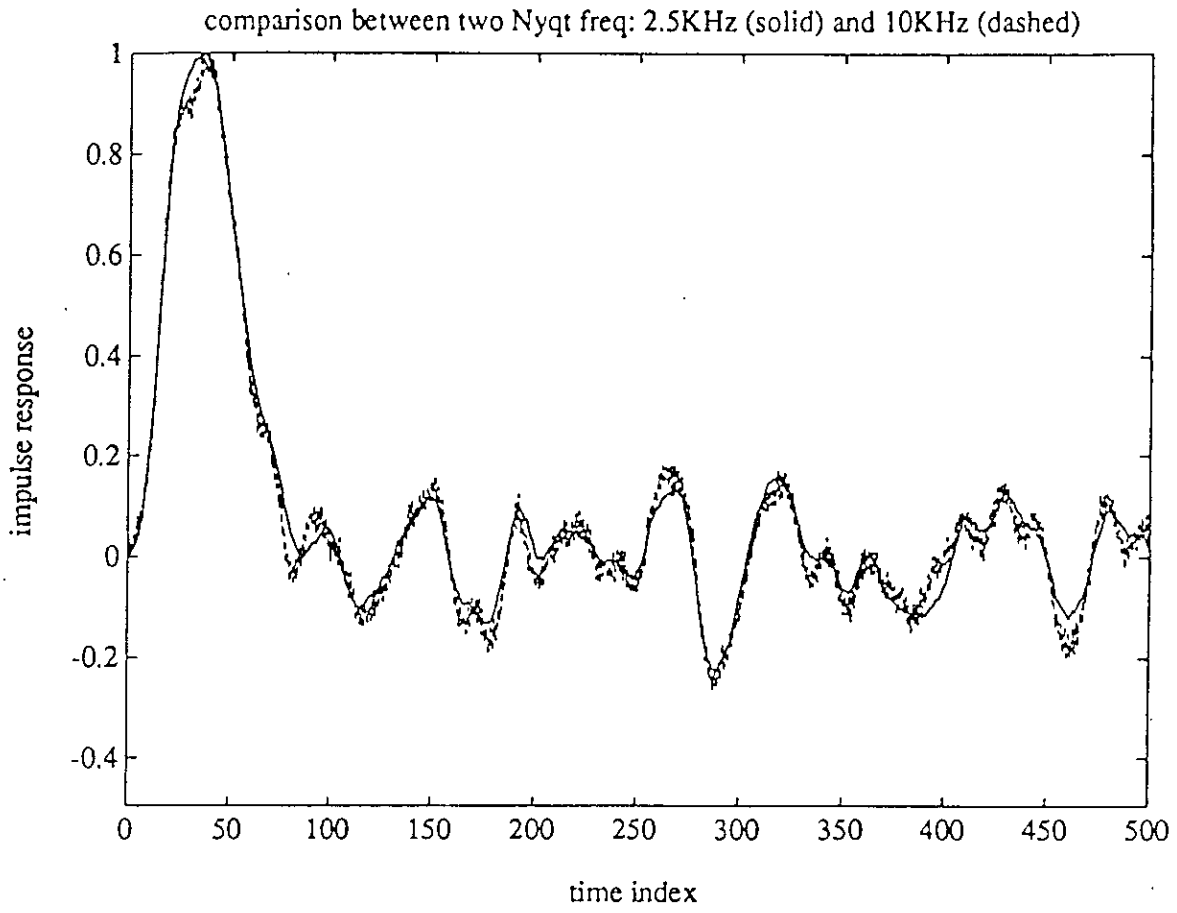

Figure 18 : Comparison of elastic impulse responses calculated by exact method using 8192 points and two Nyquist frequencies (solid : 2.5 KHz; dashed : 10 KHz).

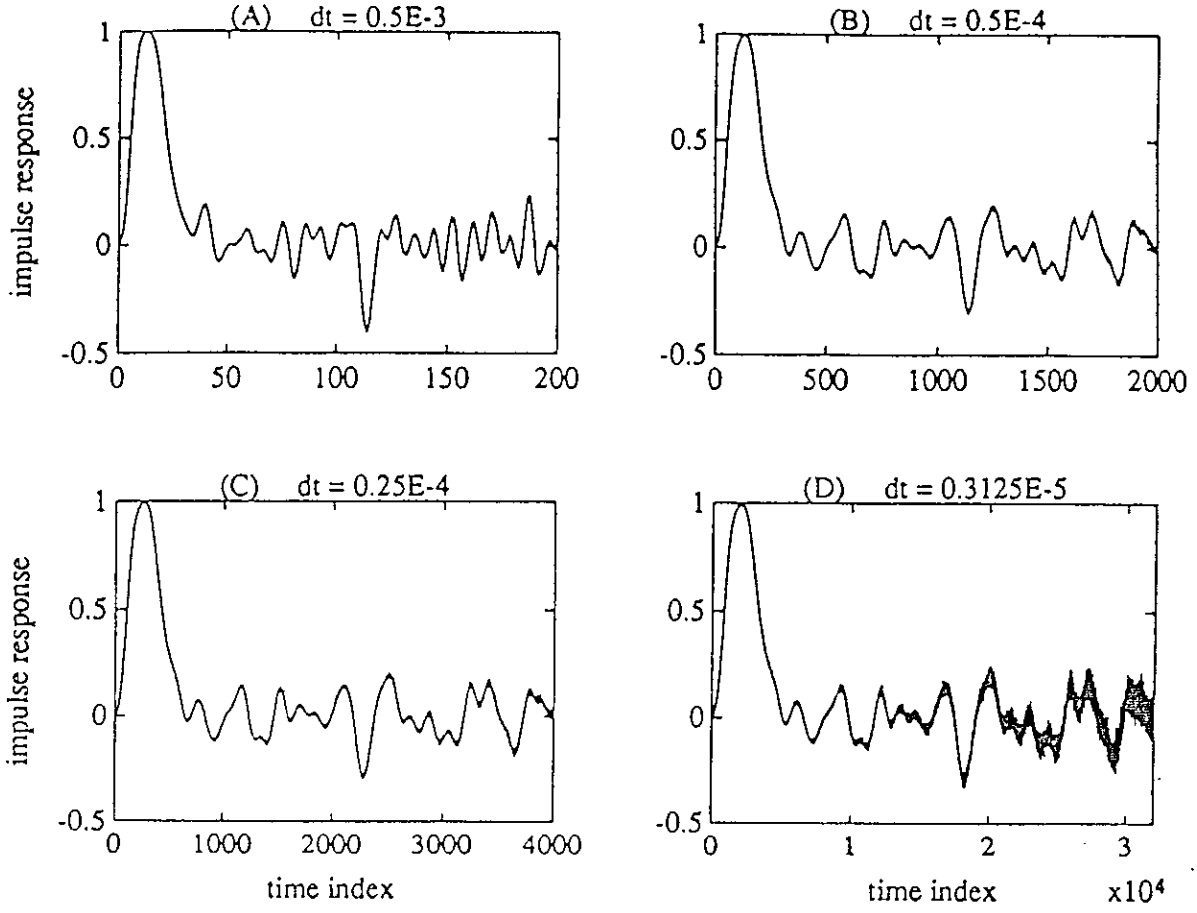

Figure 19 : Comparison of elastic impulse responses calculated by approximate method using different time steps.

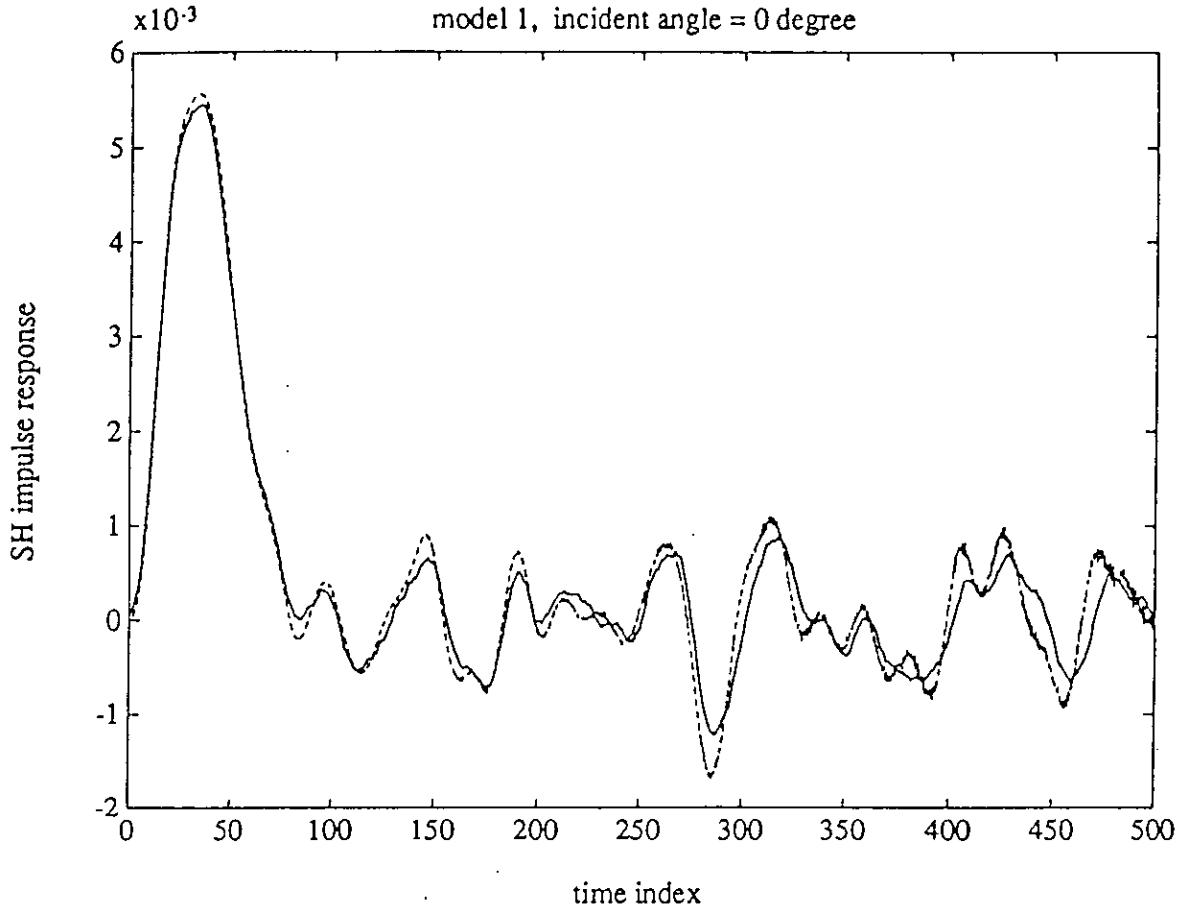

Figure 20 : Comparison of elastic impulse responses at normal incidence (solid : exact; dashed : approximate).

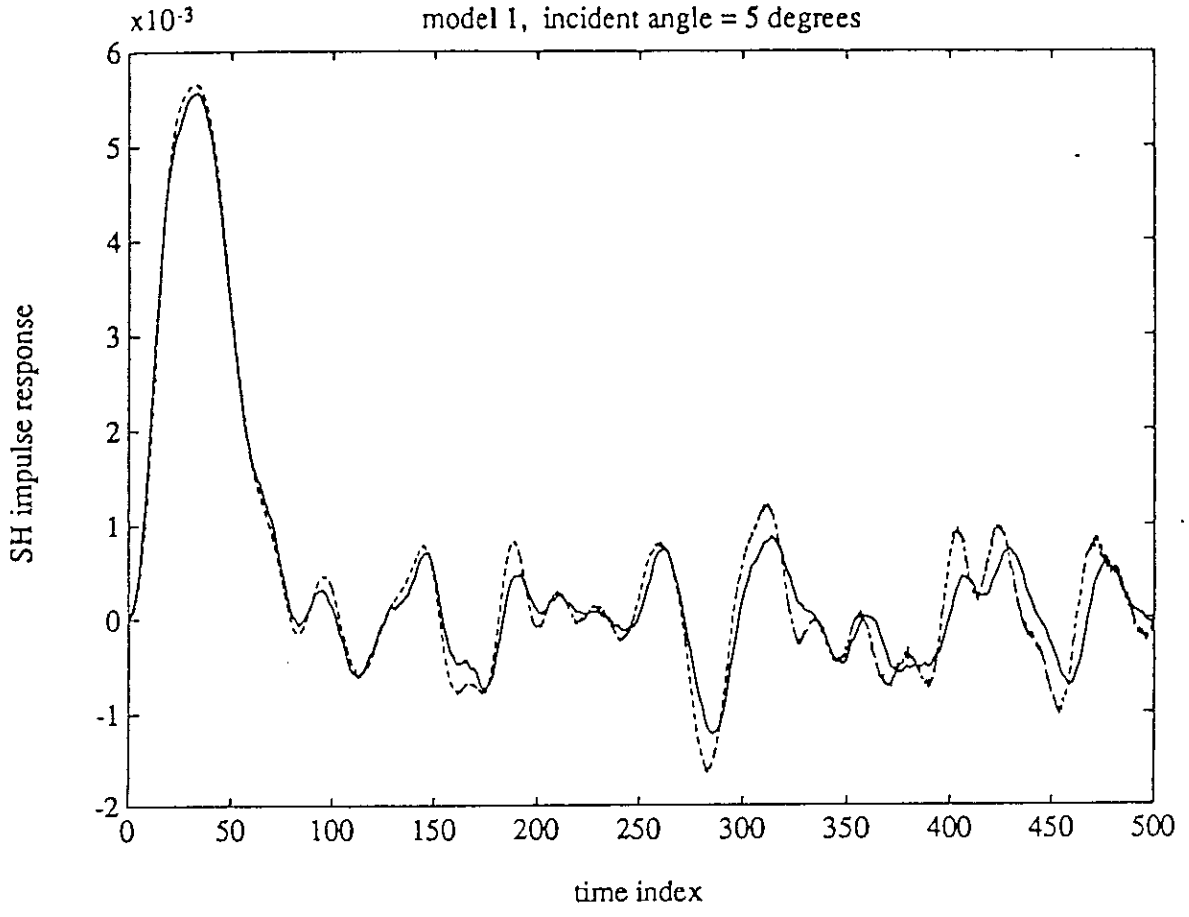

Figure 21 : Comparison of elastic impulse responses at 5^0 angle of incidence (solid : exact; dashed : approximate).

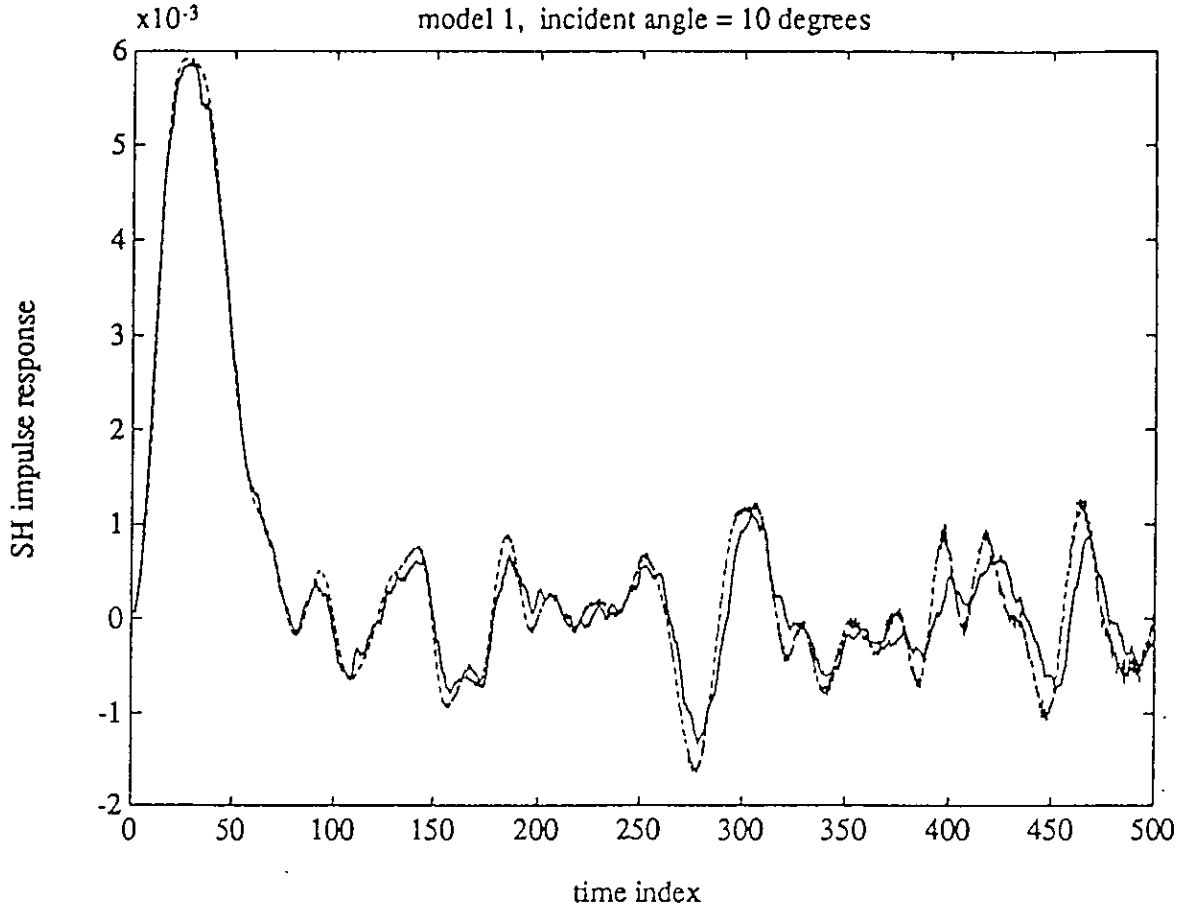

Figure 22 : Comparison of elastic impulse responses at 10^0 angle of incidence (solid : exact; dashed : approximate).

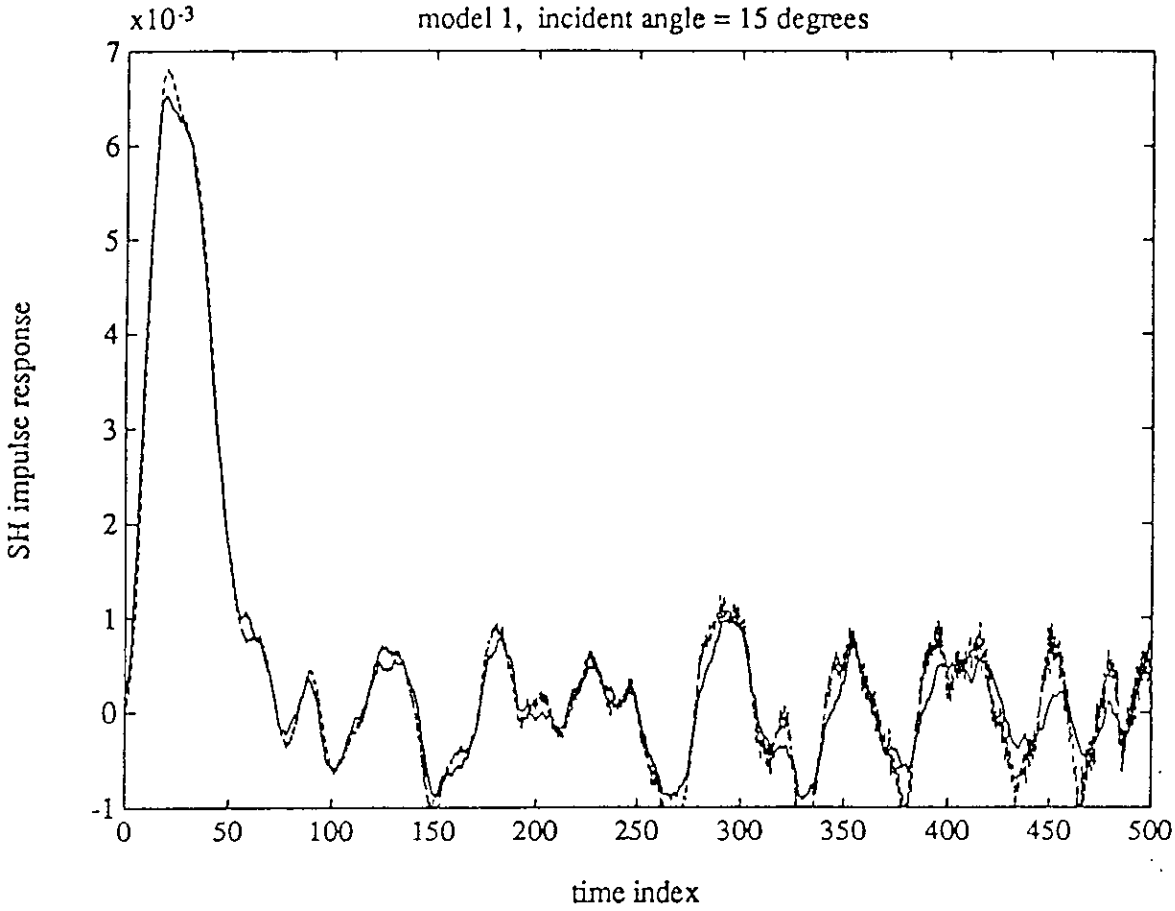

Figure 23 : Comparison of elastic impulse responses at 15^0 angle of incidence (solid : exact; dashed : approximate).

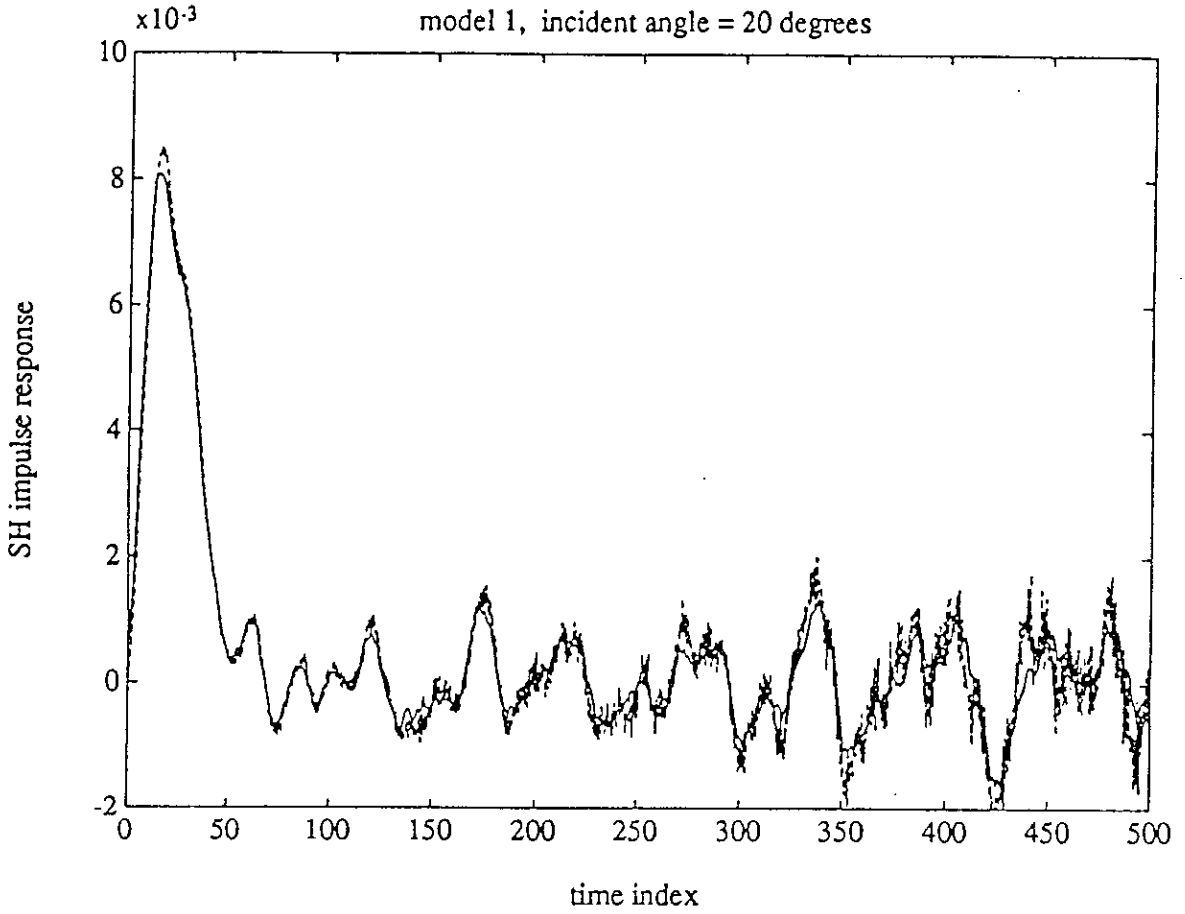

Figure 24 : Comparison of elastic impulse responses at 20o angle of incidence (solid : exact; dashed : approximate).

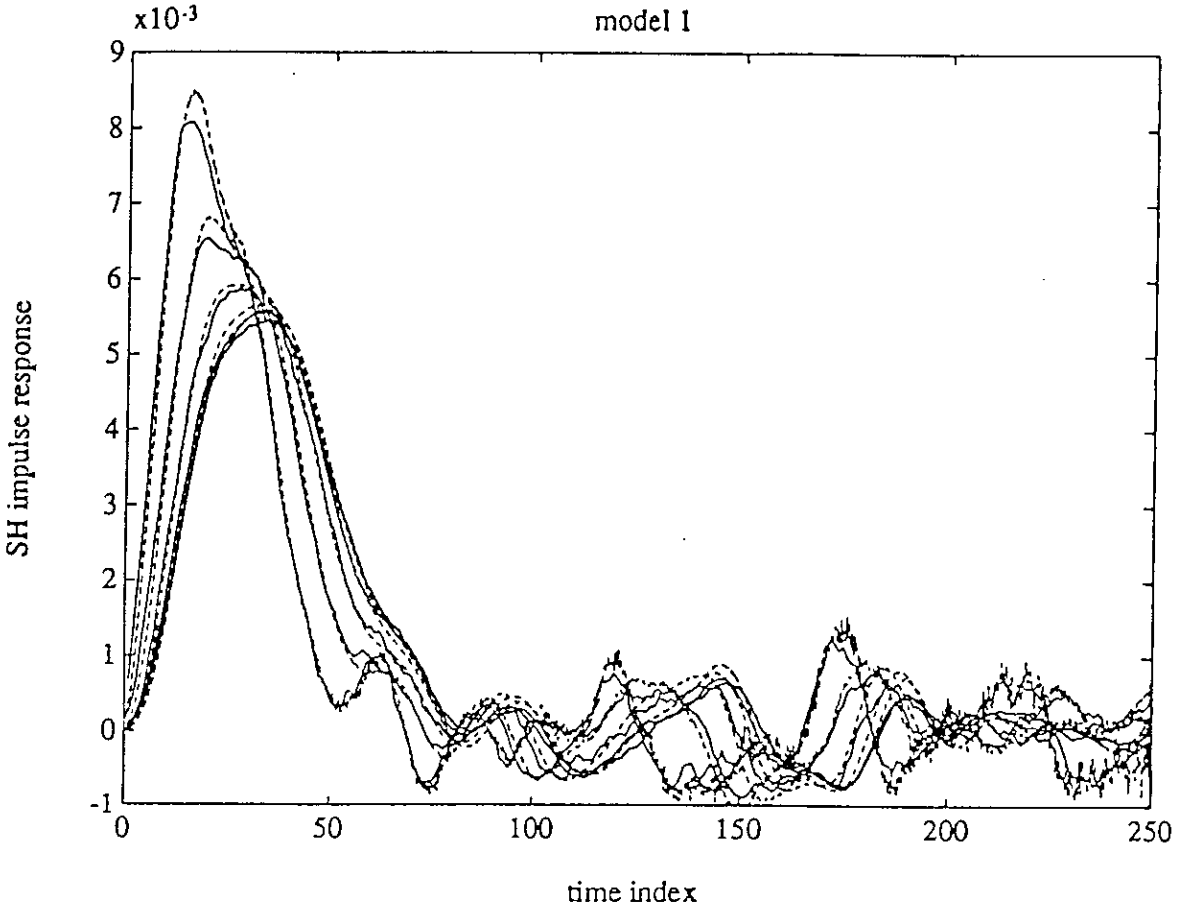

Figure 25 : Figures 20-24 plotted on the same frame (solid : exact; dashed : approximate).

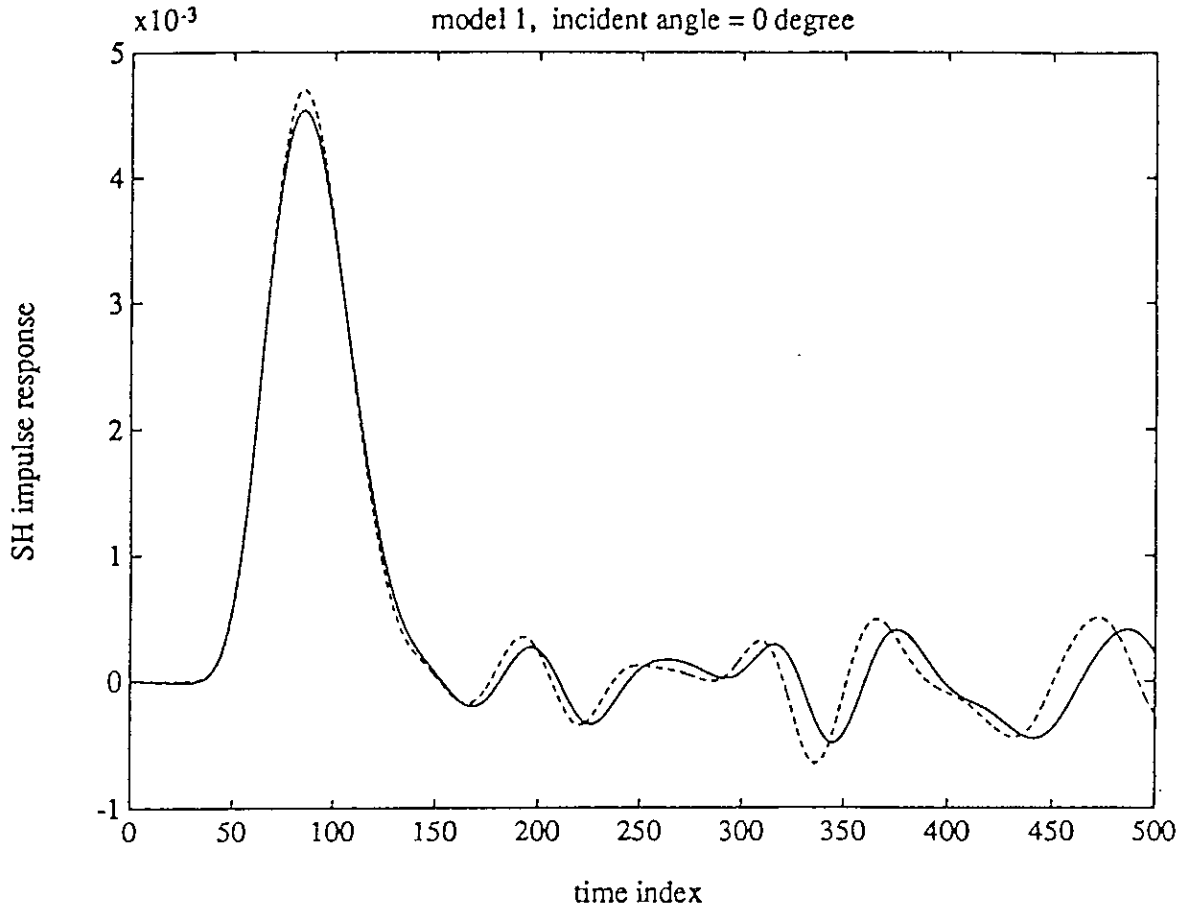

Figure 26 : Comparison of anelastic impulse responses at normal incidence (solid : exact; dashed : approximate).

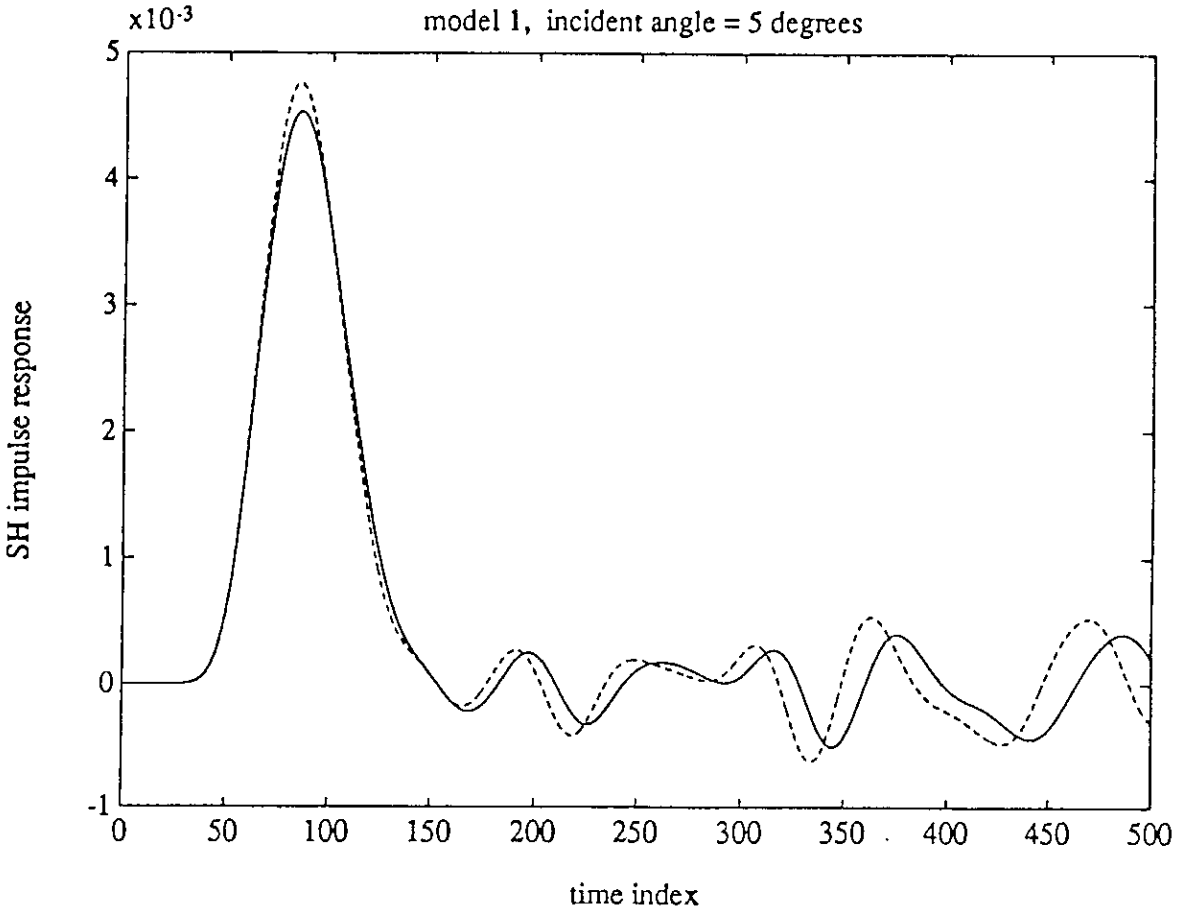

Figure 27 : Comparison of anelastic impulse responses at 5° angle of incidence (solid : exact; dashed : approximate).

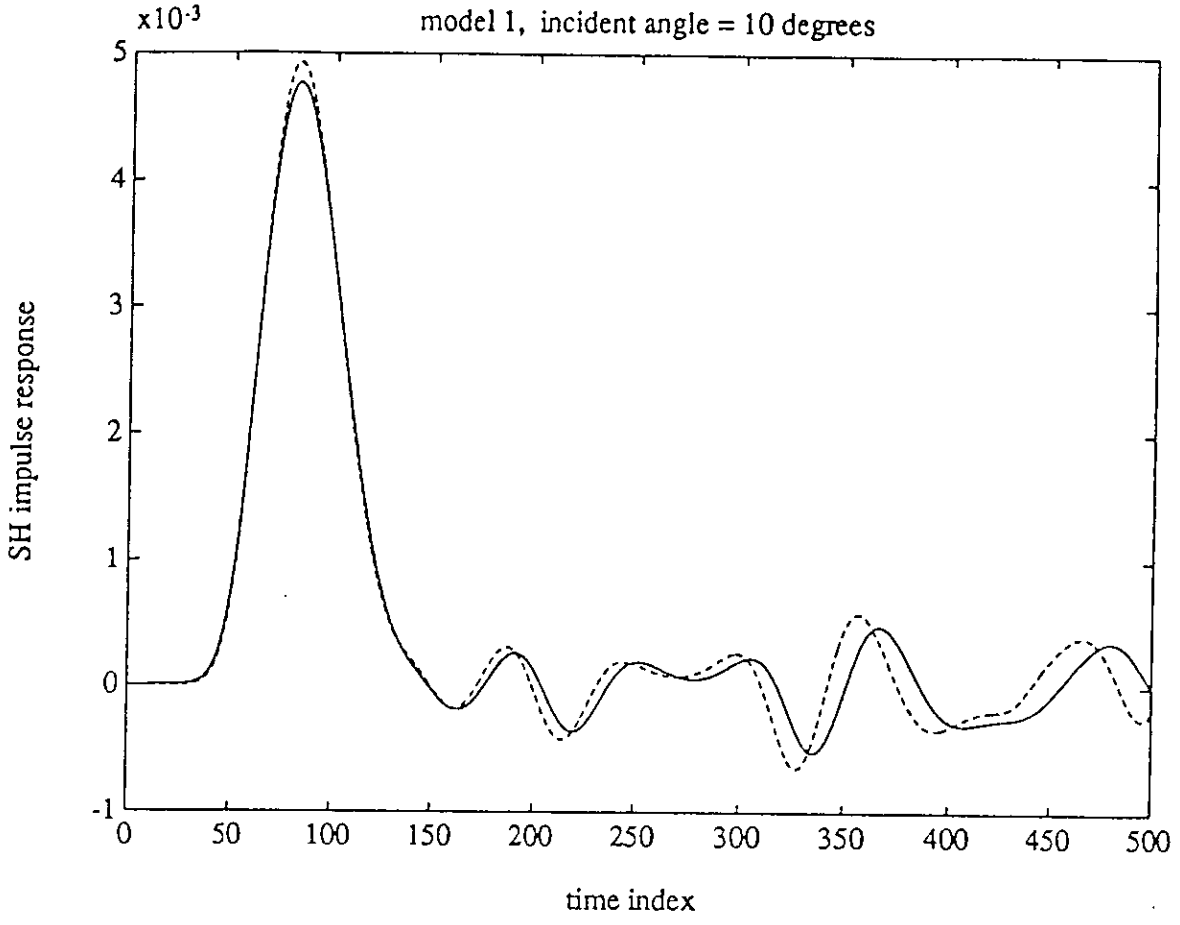

Figure 28 : Comparison of anelastic impulse responses at 10° angle of incidence (solid : exact; dashed : approximate).

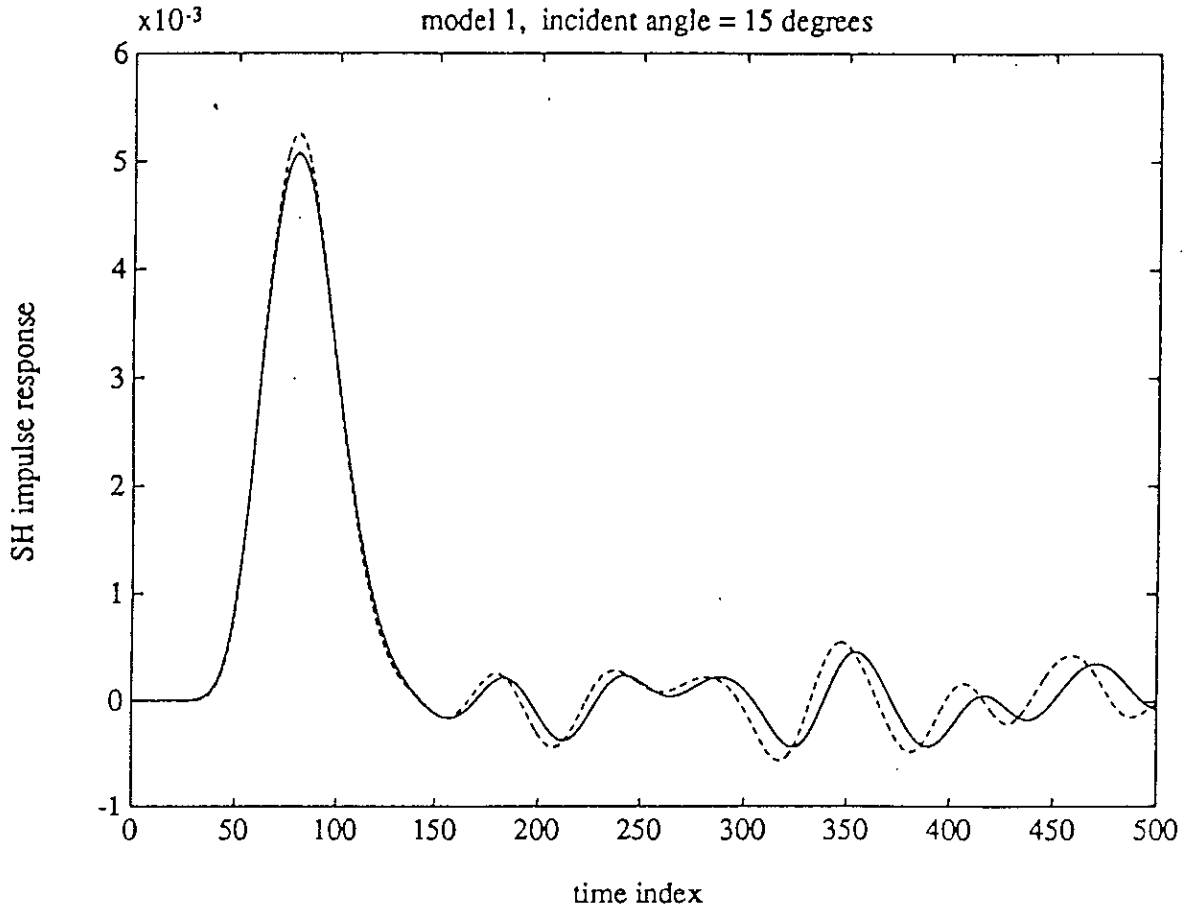

Figure 29 : Comparison of anelastic impulse responses at 15° angle of incidence (solid : exact; dashed : approximate).

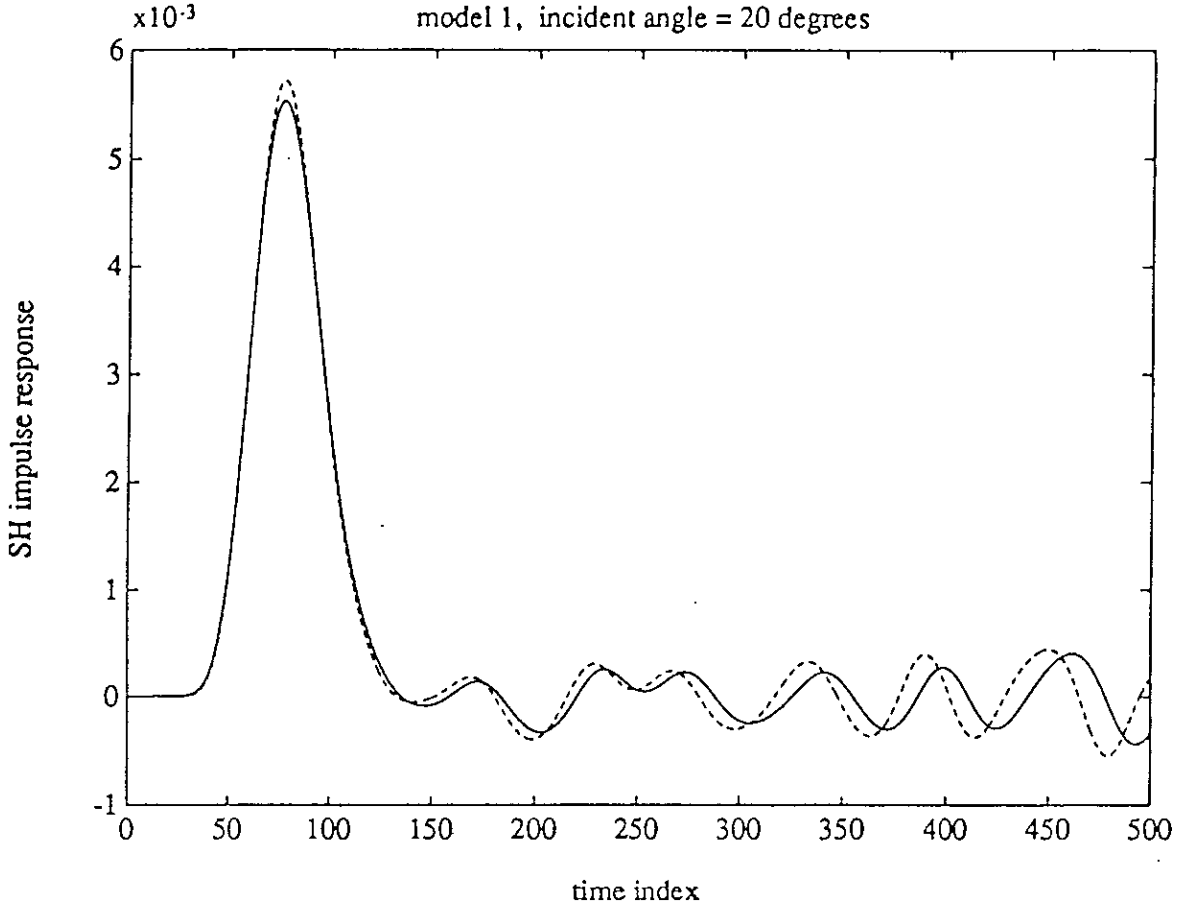

Figure 30 : Comparison of anelastic impulse responses at 20° angle of incidence (solid : exact; dashed : approximate).

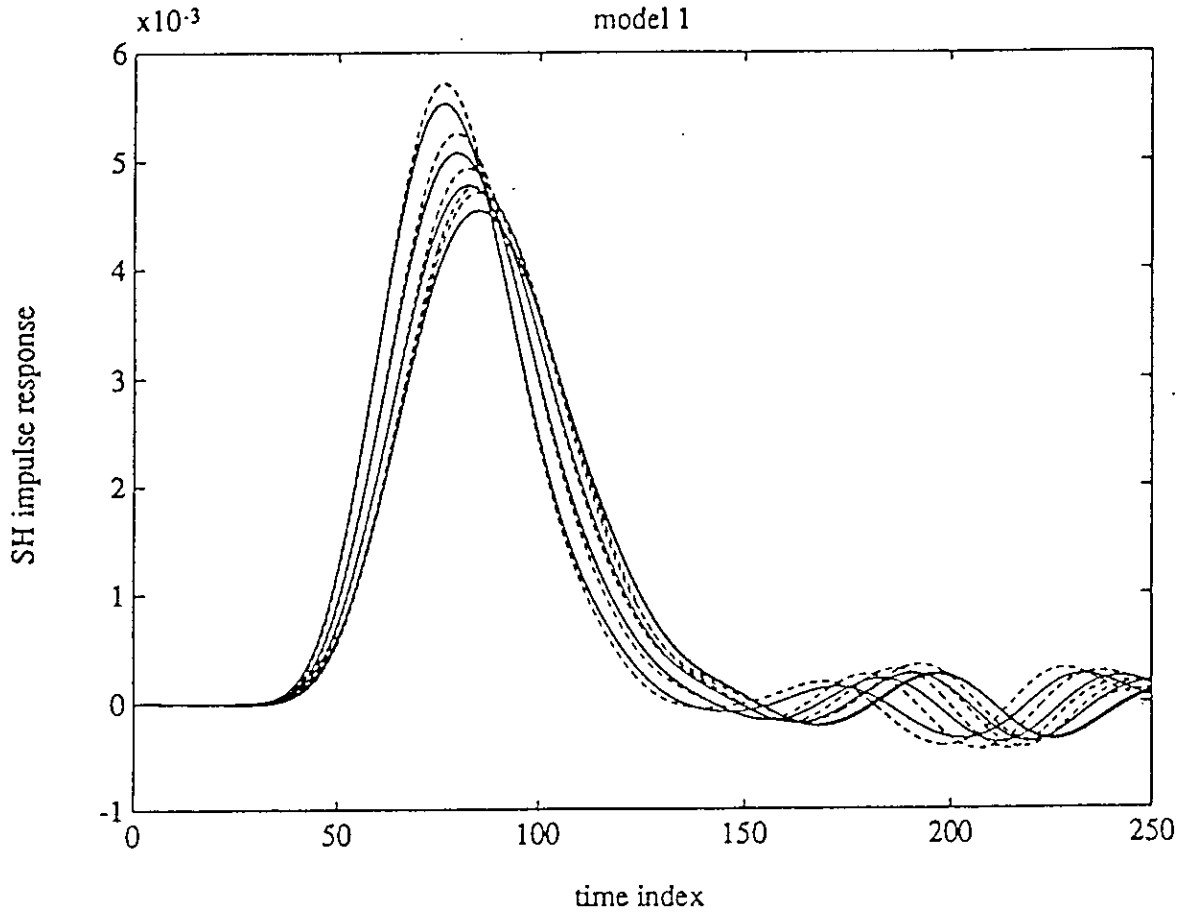

Figure 31 : Figures 26-30 plotted on the same frame (solid : exact; dashed : approximate).

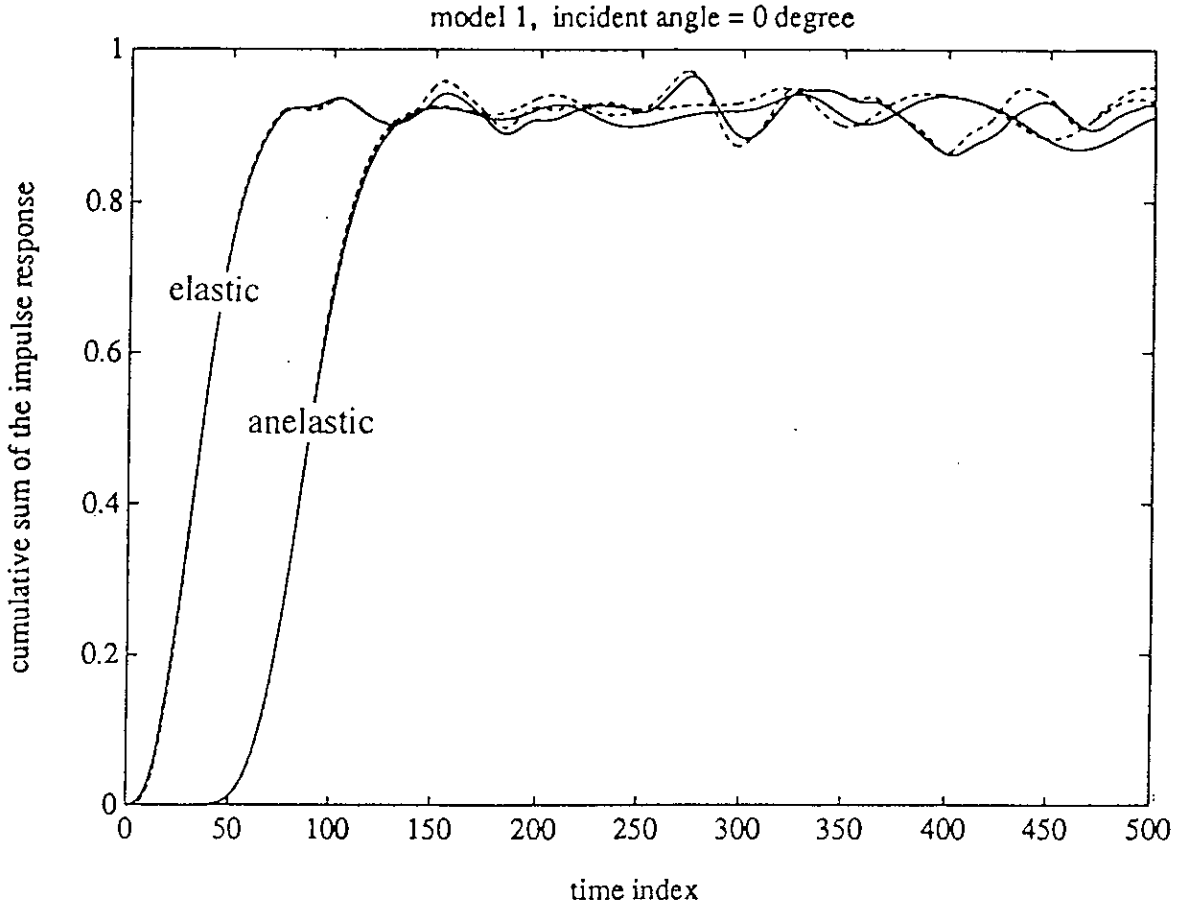

Figure 32 : Cumulative sum of the elastic and anelastic impulse responses at normal incidence (solid : exact; dashed : approximate).

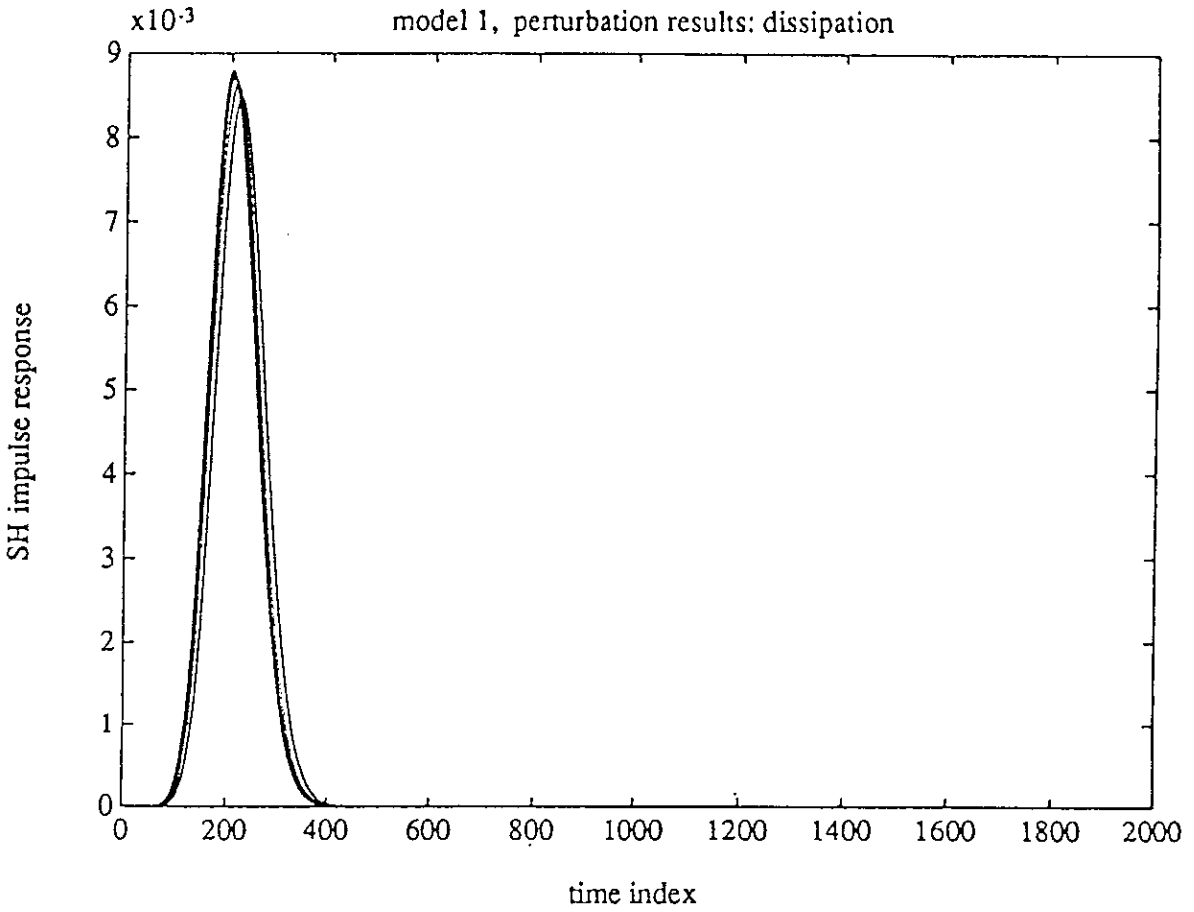

Figure 33 : Impulse responses due to dissipation only for 5 angles of incidence : 0°, 5°, 10°, 15° and 20°.